



Simulating the dynamics and interactions of flexible fibers in Stokes flows

Anna-Karin Tornberg^{*}, Michael J. Shelley

Courant Institute of Mathematical Sciences, New York University, 251 Mercer Street, NY 10012, USA

Received 11 June 2003; received in revised form 10 October 2003; accepted 20 October 2003

Abstract

The dynamics of slender filaments or fibers suspended in Stokesian fluids are fundamental to understanding many flows arising in physics, biology and engineering. Such filaments can have aspect ratios of length to radius ranging from a few tens to several thousands. Full discretizations of such 3D flows are very costly. Instead, we employ a non-local slender body theory that yields an integral equation, along the filament centerline, relating the force exerted on the body to the filament velocity. This hydrodynamical description takes into account the effect of the filament on the fluid, and is extended to capture the interaction of multiple filaments as mediated by the intervening fluid. We consider filaments that are inextensible and elastic. Replacing the force in the slender body integral equation by an explicit expression that uses Euler–Bernoulli theory to model bending and tensile forces yields an integral expression for the velocity of the filament centerlines, coupled to auxiliary integro-differential equations for the filament tensions. Based on a regularized version of these slender body equations that is asymptotically equivalent to the original formulation, we construct a numerical method which uses a combination of finite differences, implicit time-stepping to avoid severe stability constraints, and special quadrature methods for nearly singular integrals. We present simulations of single flexible filaments, as well as multiple interacting filaments, evolving in a background shear flow. These simulations show shear induced buckling and relaxation of the filaments, leading to the storage and release of elastic energy. These dynamics are responsible for the development of positive first normal stress differences, commonly associated with visco-elastic fluids that are suspensions of microscopic elastic fibers.

© 2003 Elsevier Inc. All rights reserved.

1. Suspension of fibers/filaments

The dynamics of flexible fibers or filaments¹ immersed in a fluid are important to understanding many interesting problems arising in biology, engineering, and physics. For example, flexible fibers make up the micro-structure of suspensions that show strongly non-Newtonian bulk behavior, such as elasticity, shear-

^{*} Corresponding author. Fax: +1-212-995-4121.

E-mail addresses: tornberg@cims.nyu.edu (A.-K. Tornberg), shelley@cims.nyu.edu (M.J. Shelley).

¹ In this paper, we will use the terms filament and fiber interchangeably.

thinning, and normal stresses in shear flow [13,24]; micro-organisms utilize for locomotion the anisotropic drag properties of their long flexible flagella [6]; rheological measurements have been used to probe the biophysical properties of filament-like biological polymers such as actin [10]. The dynamics of flexible filaments are also relevant to understanding soft materials. Liquid crystal phase transitions lead to the study of growing elastic filaments, [27,32], while solutions of worm-like micelles have very complicated and interesting macroscopic behavior [5,19,24]. In all these problems, the filaments have large aspect ratios (length over radius), ranging from order 10 to 1000 for natural to synthetic fibers, and up to many thousands in biological settings.

From this list of examples, it is also plain that we are concerned here with systems where inertia of both fluid and filament can be neglected, i.e. very low Reynolds number flows. Even so, this particular class of problems is difficult to solve accurately with a grid based method. To do so rigorously, one would need to solve appropriate elastic equations in the regions occupied by the filaments, fluid equations in the rest of the domain, while connecting the two through appropriate boundary conditions on velocity and stress. Due to these difficulties, several approximate methods have been developed.

One such class are the so-called *bead-models*. Here, the filament is modeled as a string of spherical beads, possibly linked by inextensible connectors. The aspect ratios are typically moderate, with the dynamics based upon moment and force balances and with the influence of the fibers on the flow field neglected [34,36]. Variants of bead models have been applied to suspensions of rigid fibers (e.g. [8,36]) and of flexible fibers (e.g. [22,34]). The treatment of non-local interactions varies from considering only lubrication forces [36], from bead–bead interactions treated the same way regardless of whether the beads belong to the same or different fibers [22], to using a slender body approximation to account for non-local interactions between rigid rods [8].

The immersed boundary method [28] has also been applied to this class of problems. In this method, a filament is discretized with connected Lagrangian markers, and their relative displacements by fluid motions are used to calculate the filament’s elastic response. Filament forces thus calculated are then distributed onto a background grid covering the computational domain, and used as forces acting upon the fluid, thus modifying the surrounding fluid flow. Stockie [35] used an immersed boundary method (at moderate Reynolds number) to simulate a single “filament” buckling in a linear shear-flow. In his treatment, the filament was treated as an infinitely thin elastic boundary in a two-dimensional flow. The filament was discretized using 40–80 Lagrangian markers, but the number of background grid points over the length of the filament was sometimes as low as 7. In this case, the fiber width is an artificial numerical width only that depends on the numerical discretization. If the fiber is to have a physical width, a fiber structure must be constructed from a bundle of intertwined elastic boundaries, see [25]. While widely applicable, a general difficulty with the immersed boundary method is the current lack of efficient schemes for implicit time-stepping so as to ameliorate the time-step constraints from elastic and tensile forces of the filament [26].

A very different approach is based on *slender body theory*, which exploits the large aspect ratio of the fibers by using the slenderness ratio, $\varepsilon = r/L$ (r is a fiber radius and L is a fiber length) as an expansion variable. The simplest and most popular version is the leading-order *local drag model* which gives a local relation between the velocity of the filament centerline and the force per unit length, \mathbf{f} , that the filament exerts on the fluid

$$8\pi\mu(\mathbf{x}_t - \mathbf{U}) = c(\mathbf{I} + \hat{\mathbf{s}}\hat{\mathbf{s}})\mathbf{f}. \quad (1)$$

Here, μ is the fluid viscosity, \mathbf{U} is a given background flow, $\hat{\mathbf{s}}$ is the tangent vector to the centerline, $\hat{\mathbf{s}}\hat{\mathbf{s}}$ is the dyadic product, and $c \sim \ln \varepsilon^{-1}$. A central example is an elastic filament where, for example, $\mathbf{f} = -E\mathbf{x}_{ssss} + \mathbf{g}$ with E the bending rigidity, for which the dynamics is then given by a fourth-order PDE. Goldstein and collaborators [11,12] have used versions of Eq. (1) to investigate the relaxational and forced dynamics of stiff polymers. In the presence of a background shear flow, Becker and Shelley [4] used a local drag model to study the flow induced buckling of a single elastic filament in the plane, and showed that instability to

buckling was associated with generation of normal stress differences. On the numerical side, we see from the local model with elastic response that the dynamics involve strong time-stepping constraints. Such constraints are also found in less approximate formulations.

The primary appeal of using a local drag model lies in its reduction of filament/fluid interaction to a relatively simple equation on the filament centerline. However, the local drag model neglects non-local hydrodynamic interactions, and while such interactions are actually of higher order in ε , they are only weakly separated from the leading order term by a factor logarithmic in ε (i.e. the next-order terms in Eq. (1) are $O(1)$). Local drag models do not include interactions mediated by the intervening incompressible fluid, be they from the filament itself or from other filaments and structures in the fluid.

Keller and Rubinow [23] have developed a non-local slender body approximation that captures the global effect on the fluid velocity arising from the presence of the filament, making use of the theory of fundamental solutions for Stokes flow. Their approach yields an integral equation with a modified Stokeslet kernel on the filament centerline that relates the filament forces to the velocity of the centerline. Johnson [21] added a more detailed analysis and a modified formulation that included accurate treatment of the filament's free ends, yielding an equation that is asymptotically accurate to $O(\varepsilon^2 \log \varepsilon)$. Götz [14] also derived a slender body approximation, and performed a detailed analysis of the case of straight filaments, and established a connection of this integral equation operator with Legendre polynomials. The major difference to local drag models is that this non-local approximation takes into account the influence of the filament on the flow field.

Shelley and Ueda [32,33] were the first to design a numerical method based on a non-local slender body approximation for simulating flexible filaments. Their interest was understanding the dynamics of a flexible filament growing everywhere along its length, motivated by observations of phase transitions in smectic-A liquid crystals wherein thermodynamic and fluid dynamic effects compete to form space-filling patterns. Their formulation and numerical methods relied strongly on the assumption that the filament was closed, i.e. had no free ends, and that the filament dynamics were constrained to a plane in 3D space.

In this work, we consider multiple, interacting slender filaments with free ends in a three-dimensional Stokes flow. For Stokes flow, boundary integral methods can be employed to reduce the three-dimensional dynamics to the dynamics of the two-dimensional filament surfaces, [30]. Using slender body asymptotics, this can be further reduced to the dynamics of the one-dimensional filament centerlines.

The result is a non-local slender body formulation that includes the effect of fluid–filament interactions, as well as filament–filament ones (as mediated by the fluid). We develop a numerical method based on this theory that allows for simulating highly flexible fibers. Since the three-dimensional problem at hand is reduced to a set of coupled one-dimensional problems on each of the filament centerlines, the number of discretization points needed for a desired resolution is much smaller than it would be for a grid based method, such as the immersed boundary method, yielding a lower computational cost. Another important fact is that the framework is suitable for introducing a semi-implicit time-stepping scheme, eliminating the severe constraint on the time-step size arising from the elasticity. Unlike the bead-models, we separate our formulation of the problem from its specific numerical treatment. This allows us to do resolution studies to check the quality of our discretization.

In Section 2, we briefly review the non-local slender body theory, and give our formulation of the problem. The filaments are assumed to be inextensible and to have finite bending rigidity, and the fiber inextensibility generates an auxiliary integro-differential equation for the fiber tension. An analysis for straight filaments shows that the original formulation of the slender body equations is not suitable for numerical simulations (see Appendix B), and an appropriate regularization that does not change the asymptotic accuracy of the formulation is introduced in Section 2.4.

We further develop numerical methods for simulating filament dynamics, discussed in Section 3. Our approach is based on second-order divided differences for spatial derivatives, combined with special product integration methods that reflect the nearly singular nature of the integral operators (Section 3.1).

Despite the presence in the dynamics of terms with many spatial derivatives, stable time-stepping with only a first-order constraint on the time-step size is achieved by a mixed explicit/implicit treatment of the dynamics (Section 3.2). Several other issues are discussed, such as imposing spatial periodicity in our simulations, the proper treatment of filament interactions, and demonstrating second-order convergence in our simulations. We present illustrative numerical simulations for the dynamics of a single filament, and for 25 interacting filaments, set within background shearing flows (Sections 4.1 and 4.2).

2. Problem formulation

2.1. Non-local slender body approximation

The flows we are considering are at very low Reynolds numbers, so it is appropriate to consider the Stokes equations. Denote the velocity field by $\mathbf{u}(\mathbf{x})$, the pressure by $p(\mathbf{x})$, and let $\mathbf{f}(\mathbf{x})$ be a force acting on the fluid, where $\mathbf{x} = (x, y, z) \in \mathbb{R}^3$. The Stokes equations read

$$\nabla p - \mu \Delta \mathbf{u} = \mathbf{f} \quad \text{in } \Omega,$$

$$\nabla \cdot \mathbf{u} = 0 \quad \text{in } \Omega,$$

where μ is the viscosity of the fluid.

Now, assume we have a filament in the flow, and let Γ denote its surface and \mathbf{u}_Γ its surface velocity. We impose the no-slip condition on Γ and require that far away $\mathbf{u}(\mathbf{x})$ is equal to a background velocity $\mathbf{U}_0(\mathbf{x})$, also a solution to the Stokes equations. Hence,

$$\mathbf{u} = \mathbf{u}_\Gamma \quad \text{on } \Gamma, \quad \mathbf{u} \rightarrow \mathbf{U}_0 \quad \text{for } \|\mathbf{x}\| \rightarrow \infty.$$

In the case of several filaments this can be generalized by considering the union of all filament surfaces, and imposing no-slip conditions thereon.

A full boundary integral formulation for this problem would yield integral equations on the surfaces of the filaments [30]. For slender filaments, such a formulation would be very expensive to solve numerically. Instead, we use the filament slenderness to reduce the integral equations to the filament centerlines. This is done using fundamental solutions to the Stokes equations.

One such fundamental solution is the Stokeslet. If $\mathbf{f} = \delta(\mathbf{x})\mathbf{e}_i$, with \mathbf{e}_i the unit vector in direction i , then $\mathbf{u}(\mathbf{x}) = \mathbf{Y}(\mathbf{x}, \mathbf{0})\mathbf{e}_i$ is a solution to the Stokes equations, with the Stokeslet tensor given by

$$\mathbf{Y}(\mathbf{x}, \mathbf{x}_0) = \frac{1}{8\pi\nu} \frac{\mathbf{I} + \hat{\mathbf{R}}\hat{\mathbf{R}}}{|\mathbf{R}|},$$

where \mathbf{I} is the identity tensor, $\mathbf{R} = \mathbf{x} - \mathbf{x}_0$ and $\hat{\mathbf{R}}$ the unit vector $\hat{\mathbf{R}} = \mathbf{R}/|\mathbf{R}|$.

In addition to the Stokeslet, higher order fundamental solutions can be constructed by differentiation. The so-called doublet is defined as

$$\mathbf{Y}_2(\mathbf{x}, \mathbf{x}_0) = \frac{1}{2} \Delta \mathbf{Y}(\mathbf{x}, \mathbf{x}_0) = \frac{1}{8\pi\nu} \frac{\mathbf{I} - 3\hat{\mathbf{R}}\hat{\mathbf{R}}}{|\mathbf{R}|^3}.$$

A non-local slender body approximation can be derived by placing fundamental solutions (Stokeslets and doublets) on the filament centerline, then applying the technique of matched asymptotics to derive the approximate equation. This step is very involved since it requires an inner as well as an outer expansion, and then a reformulation of the outer expansion in the inner variables, so that a matching can be made. The

formulation is closed by enforcing a no-slip condition on the filament surface, assuming the velocity to be a function of arclength only, i.e. that there is no angular variation in filament velocity. In all this, higher order terms in the slenderness parameter ε have been neglected, and the final equation for the velocity of the filament centerline is of order $O(\varepsilon^2 \log \varepsilon)$. This accuracy holds also for a filament with free ends, if the ends are tapered [21]. For details on the derivation, see [14,21,23].

This yields an integral equation for the centerline of the filament, which includes the effect on the flow by the presence of the filament.

2.2. The slender body equations

Let the centerline of a filament be parameterized by arclength $s \in [0, L]$, where L is the length of the filament and let $\mathbf{x}(s, t) = (x(s, t), y(s, t), z(s, t))$ be the coordinates of the filament centerline. In the cases we consider, the arclength s is a material parameter for the filament, so that it is independent of t .

Assuming that the filament does not reapproach itself, and that the radius of the filament is given by $r(s) = 2\varepsilon\sqrt{s(L-s)}$, so that $r(L/2) = \varepsilon L$, a non-local slender body approximation [14,21] of the velocity of the filament centerline is given by

$$8\pi\mu \left(\frac{\partial \mathbf{x}(s, t)}{\partial t} - \mathbf{U}_0(\mathbf{x}(s, t), t) \right) = -\mathcal{A}[\mathbf{f}](s) - \mathbf{K}[\mathbf{f}](s), \quad (2)$$

where \mathbf{f} is the force per unit length on the filament. The local operator \mathcal{A} is given by

$$\mathcal{A}[\mathbf{f}](s) = [-c(\mathbf{I} + \hat{\mathbf{s}}\hat{\mathbf{s}}(s)) + 2(\mathbf{I} - \hat{\mathbf{s}}\hat{\mathbf{s}}(s))]\mathbf{f}(s), \quad (3)$$

and the integral operator $\mathbf{K}[\mathbf{f}](s)$ is given by

$$\mathbf{K}[\mathbf{f}](s) = \int_0^L \left(\frac{\mathbf{I} + \hat{\mathbf{R}}(s, s')\hat{\mathbf{R}}(s, s')}{|\mathbf{R}(s, s')|} \mathbf{f}(s') - \frac{\mathbf{I} + \hat{\mathbf{s}}(s)\hat{\mathbf{s}}(s)}{|s - s'|} \mathbf{f}(s) \right) ds'. \quad (4)$$

Here, $\mathbf{R}(s, s') = \mathbf{x}(s) - \mathbf{x}(s')$, and $\hat{\mathbf{R}}\hat{\mathbf{R}}$ and $\hat{\mathbf{s}}\hat{\mathbf{s}}$ are dyadic products, i.e. $(\hat{\mathbf{R}}\hat{\mathbf{R}})_{kl} = \hat{\mathbf{R}}_k \hat{\mathbf{R}}_l$. The constant $c = \log(\varepsilon^2 e)$, $c < 0$, where $\varepsilon = r(L/2)/L$ is the slenderness parameter. The operator $\mathbf{K}[\mathbf{f}](s)$ is a so-called finite part integral; each term in the integrand is singular at $s' = s$, and the integral is only well defined when the integrand is kept as the difference of its two terms.

Note that the operators \mathcal{A} and \mathbf{K} depend on the shape of the filament, as given by $\mathbf{x}(s, t)$, even though this is not explicitly indicated in the notation. In Eq. (2), the operator $-c(\mathbf{I} + \hat{\mathbf{s}}\hat{\mathbf{s}}(s))$ is that arising in local slender body theory. The remainder includes non-local corrections which capture the global effect on the fluid velocity from the presence of the filament. Johnson [21] showed that with this specific choice of the radius ($r(s) = 2\varepsilon\sqrt{s(L-s)}$), formula (2) is uniformly accurate all the way out to, and including, the end points of the filament.

Now, let \mathbf{x} be any field point, not on the filament. The fluid velocity $\mathbf{U}(\mathbf{x})$ in this point is approximated by

$$8\pi\mu(\mathbf{U}(\mathbf{x}) - \mathbf{U}_0(\mathbf{x})) = - \int_0^L \left[\frac{\mathbf{I} + \hat{\mathbf{R}}(s')\hat{\mathbf{R}}(s')}{|\mathbf{R}(s')|} + \frac{\varepsilon^2}{2} \frac{\mathbf{I} - 3\hat{\mathbf{R}}(s')\hat{\mathbf{R}}(s')}{|\mathbf{R}(s')|^3} \right] \mathbf{f}(s') ds', \quad (5)$$

where now $\mathbf{R}(s') = \mathbf{x} - \mathbf{x}(s')$; see [14]. Note that the second part of the integral will be negligible at all but very small distances from the filament.

Eq. (2) gives the equation of motion for one filament subject to a background flow, given that the force acting on the filament is known. The equation for the velocity at a field point (5) tells us how the presence of one filament contributes to the total velocity field. If there are more filaments, the contributions from these

filaments simply add, due to the superposition principle for linear Stokes flow. Hence, the background flow for a filament that is interacting with other filaments will simply be modified with the contributions from the other filaments; the other parts of Eq. (2) will stay the same.

While the asymptotic accuracy of Eq. (2) is $O(\varepsilon^2 \log \varepsilon)$, the formula for the velocity field (5) is only accurate to $O(\varepsilon)$. Formally, the equations for multiple interacting filaments are therefore accurate to $O(\varepsilon)$, even though the most important contribution for each filament, i.e. the one from the filament itself, is computed to $O(\varepsilon^2 \log \varepsilon)$.

When there are several filaments, we introduce an indexing and denote the filaments by Γ_l , $l = 1, \dots, M$, and the filament coordinates by $\mathbf{x}_l(s, t) = (x_l(s, t), y_l(s, t), z_l(s, t))$. For filament Γ_l , we have

$$8\pi\mu \left(\frac{\partial \mathbf{x}_l(s, t)}{\partial t} - \mathbf{U}_0(\mathbf{x}_l(s, t), t) \right) = -\mathbf{A}_l[\mathbf{f}_l](s) - \mathbf{K}_l[\mathbf{f}_l](s) - \sum_{k=1, k \neq l}^M \left[\mathbf{V}_k(\mathbf{x}_l(s)) + \frac{\varepsilon^2}{2} \mathbf{W}_k(\mathbf{x}_l(s)) \right], \quad (6)$$

where we sum over $\mathbf{V}_k(\mathbf{x}_l(s)) + (\varepsilon^2/2)\mathbf{W}_k(\mathbf{x}_l(s))$, the contribution from all other filaments to the velocity at filament l . In particular,

$$\mathbf{V}_k(\bar{\mathbf{x}}) = \int_{\Gamma_k} \left[\frac{\mathbf{I} + \hat{\mathbf{R}}_k(s') \hat{\mathbf{R}}_k(s')}{|\mathbf{R}_k(s')|} \right] \mathbf{f}_k(s') \, ds', \quad (7)$$

and

$$\mathbf{W}_k(\bar{\mathbf{x}}) = \int_{\Gamma_k} \left[\frac{\mathbf{I} - 3\hat{\mathbf{R}}_k(s') \hat{\mathbf{R}}_k(s')}{|\mathbf{R}_k(s')|^3} \right] \mathbf{f}_k(s') \, ds'. \quad (8)$$

where $\mathbf{R}_k(s') = \bar{\mathbf{x}} - \mathbf{x}_k(s')$, and $\hat{\mathbf{R}}$ is the normalized \mathbf{R} -vector, as usual.

The integral defining $\mathbf{V}_k(\bar{\mathbf{x}})$ in the sum appears at first glance to decay as $1/|\mathbf{R}|$. However, in the cases we study here, the filaments are so-called “force free” particles [2], and the specific form of \mathbf{f} will imply that the decay of $\mathbf{V}_k(\bar{\mathbf{x}})$ is actually $1/|\mathbf{R}|^2$ and that the decay of $\mathbf{W}_k(\bar{\mathbf{x}})$ is $1/|\mathbf{R}|^4$. This is discussed in Section 2.5.

2.3. Completing the formulation

For simplicity, we first discuss the case of a single filament. Eq. (2) is an integral equation that relates the filament velocity to the forces acting on the filament. Here, we will assume that the filament forces can be described by Euler–Bernoulli elasticity [31], and take

$$\mathbf{f}(s) = -(T(s)\mathbf{x}_s)_s + E\mathbf{x}_{ssss}. \quad (9)$$

Here, we denote derivatives with respect to arclength with a subscript s , thus giving $\mathbf{x}_s = \hat{\mathbf{s}}$ and $\mathbf{x}_{ss} = \kappa\hat{\mathbf{n}}$, with $\hat{\mathbf{n}}$ the principal normal. The first term in Eq. (9) is the filament tensile forces, with T the tension, which resists compression and extension. The line tension $T(s)$ will act as a Lagrange multiplier ensuring that the filament remains inextensible. The second term represents bending forces, with E the rigidity. Twist elasticity is neglected [12]. The ends of the filament are “free”, that is, no forces or moments are exerted on them, so that $\mathbf{x}_{ss}|_{s=0,L} = \mathbf{x}_{ssss}|_{s=0,L} = 0$ and $T|_{s=0,L} = 0$. Note that $\mathbf{f}(s) = (d/ds)\mathbf{F}(s)$, where $\mathbf{F}(s) = -T(s)\mathbf{x}_s + E\mathbf{x}_{sss}$, and so $\mathbf{F}(0) = \mathbf{F}(L) = 0$.

Assuming $\mathbf{U}_0(\mathbf{x}, t)$ to be a shear flow of strength $\dot{\gamma}$, we non-dimensionalize the problem using the length L , time $t = \dot{\gamma}^{-1}$, and force $F = E/L^2$. The non-dimensional equations are controlled by two parameters, an effective viscosity

$$\bar{\mu} = \frac{8\pi\mu\dot{\gamma}L^2}{E/L^2}, \quad (10)$$

which represents a ratio between the characteristic fluid drag and the filament elastic force, and the asymptotic parameter $c = \log(\varepsilon^2 e)$.

Now, consider the assumption of inextensibility. Since the filament is inextensible, s will remain a material parameter, and thus s and t derivatives can always be interchanged. Hence,

$$\partial_t(\mathbf{x}_s \cdot \mathbf{x}_s) = 0 \Rightarrow \mathbf{x}_s \cdot \mathbf{x}_{ts} = 0. \quad (11)$$

This condition can be combined with Eq. (2) to derive an equation for the line tension, using Eq. (9). This yields

$$-\mathbf{x}_s \cdot \frac{\partial}{\partial s} \{ \mathcal{A}[(T\mathbf{x}_s)_s] + \mathbf{K}[(T\mathbf{x}_s)_s] \} = \mathbf{x}_s \cdot \frac{\partial}{\partial s} \{ \bar{\mu}\mathbf{U}_0 - \mathcal{A}[\mathbf{x}_{ssss}] + \mathbf{K}[\mathbf{x}_{ssss}] \},$$

which can be expanded using the definition of the local operator \mathcal{A} , and simplified using the following ladder of differential identities, derived from $\mathbf{x}_s \cdot \mathbf{x}_s = 1$,

$$\mathbf{x}_s \cdot \mathbf{x}_{ss} = 0, \quad \mathbf{x}_s \cdot \mathbf{x}_{sss} = -\mathbf{x}_{ss} \cdot \mathbf{x}_{ss}, \quad \mathbf{x}_s \cdot \mathbf{x}_{ssss} = -3\mathbf{x}_{ss} \cdot \mathbf{x}_{sss}. \quad (12)$$

The resulting simplified equation reads

$$\begin{aligned} 2cT_{ss} + (2-c)T(\mathbf{x}_{ss} \cdot \mathbf{x}_{ss}) - \mathbf{x}_s \cdot \frac{\partial}{\partial s} \mathbf{K}[(T\mathbf{x}_s)_s] &= \bar{\mu}\mathbf{x}_s \cdot \frac{\partial}{\partial s} \mathbf{U}_0 + (2-7c)(\mathbf{x}_{ss} \cdot \mathbf{x}_{sss}) - 6c(\mathbf{x}_{sss} \cdot \mathbf{x}_{ssss}) \\ &\quad - \mathbf{x}_s \cdot \frac{\partial}{\partial s} \mathbf{K}[\mathbf{x}_{ssss}]. \end{aligned} \quad (13)$$

The line tension $T(s)$ acts as a Lagrangian multiplier, constraining the motion of the filament to obey the inextensibility condition. However, the equation for $T(s)$ was derived assuming that the filament is of exactly the correct length, and hence $\mathbf{x}_s \cdot \mathbf{x}_s = 1$ for all s . However, if there is a small length error present, this error will not be corrected. On the contrary, the computed line tension could, depending on the configuration, even act so as to increase this error.

In practice, numerical errors will be introduced into our computations, and we must therefore stabilize the constraint. We replace the inextensibility condition (11) by

$$\frac{1}{2}\partial_t(\mathbf{x}_s \cdot \mathbf{x}_s) = \mathbf{x}_s \cdot \mathbf{x}_{ts} = \bar{\mu}\beta(1 - \mathbf{x}_s \cdot \mathbf{x}_s), \quad (14)$$

which is equivalent to the original condition when $\mathbf{x}_s \cdot \mathbf{x}_s = 1$, but which will act to remove the length error if there is one.

The only modification of the equation for the line tension equation (13) is the appearance of an extra term in the right-hand side: $-\bar{\mu}\beta(1 - \mathbf{x}_s \cdot \mathbf{x}_s)$. In this way the length error is penalized, and the parameter β is referred to as the penalization parameter. The line tension equation is given in full in Eq. (22).

2.4. Regularization of the integral kernel

An analysis of the straight filament case (see Appendix B) yields that the original slender body equation is not suitable for numerical computations. This can be seen as a solvability condition for the line tension equation that is not easily avoided for all ε values of interest, and hence, since that equation is derived from the time dependent equation, there are naturally related problems in computing the dynamics.

As a remedy to this, while at the same time retaining the same asymptotic accuracy as the original formulation, we introduce a regularized integral operator $\mathbf{K}_\delta[\mathbf{f}]$, defined as

$$\mathbf{K}_\delta[\mathbf{f}](s) = \int_0^1 \left(\frac{\mathbf{I} + \hat{\mathbf{R}}(s, s')\hat{\mathbf{R}}(s, s')}{\sqrt{|\mathbf{R}(s, s')|^2 + \delta(s)^2}} \mathbf{f}(s') - \frac{\mathbf{I} + \hat{\mathbf{s}}(s)\hat{\mathbf{s}}(s)}{\sqrt{|s - s'|^2 + \delta(s)^2}} \mathbf{f}(s) \right) ds', \quad (15)$$

where $\delta(s) = \delta_0\phi(s)$, where $\delta_0 = m\varepsilon$, $m > \sqrt{2}$, and $\phi(s) \in C^1(s)$ is given by

$$\phi(s) = \begin{cases} v(s/\gamma), & 0 \leq s < \gamma, \\ 1, & \gamma \leq s \leq 1 - \gamma, \\ v((1-s)/\gamma), & 1 - \gamma < s \leq 1, \end{cases} \quad (16)$$

where $v(\xi) = \xi^2(3 - 2\xi)$. The higher regularity of $\phi(s)$ is motivated by the fact that we will compute derivatives of the integral operator in the line tension equation.

The regularized integral in Eq. (15) differs by $O(\delta_0^2 \log \delta)$ to the unregularized one ($\delta = 0$). The outline for this proof is given in Appendix B, where we also motivate the choice of δ_0 .

2.5. Filament interaction

In the case of multiple filaments, the dynamics of one filament is coupled to all others through the sum over $\mathbf{V}_k(\mathbf{x}_l(s))$ and $\mathbf{W}_k(\mathbf{x}_l(s))$ in Eq. (6), where $\mathbf{V}_k(\mathbf{x}_l(s))$ and $\mathbf{W}_k(\mathbf{x}_l(s))$ were defined in Eqs. (7) and (8).

The force $\mathbf{f}_k(s)$ is a perfect derivative, i.e. $\mathbf{f}_k(s) = (\partial/\partial s)\mathbf{F}_k(s)$, where $\mathbf{F}_k(s) = -T_k(\mathbf{x}_k)_s + (\mathbf{x}_k)_{sss}$. Recall that $\mathbf{F}_k(s)|_{s=0,1} = 0$, due to the boundary conditions on T_k and $(\mathbf{x}_k)_{sss}$. Integrating by parts, Eq. (7) can be rewritten as

$$\mathbf{V}_k(\bar{\mathbf{x}}) = - \int_{\Gamma_k} \frac{(\hat{\mathbf{R}}_k \cdot (\mathbf{x}_k)_s)(\mathbf{I} + 3\hat{\mathbf{R}}_k\hat{\mathbf{R}}_k) - ((\mathbf{x}_k)_s\hat{\mathbf{R}}_k + \hat{\mathbf{R}}_k(\mathbf{x}_k)_s)}{|\mathbf{R}_k|^2} \mathbf{F}_k(s') ds', \quad (17)$$

where again $\mathbf{R}_k(s') = \bar{\mathbf{x}} - \mathbf{x}_k(s')$, and $\hat{\mathbf{R}}$ is the normalized \mathbf{R} -vector. The formula above for $\mathbf{V}_k(\bar{\mathbf{x}})$ explicitly shows the $1/|\mathbf{R}|^2$ decay of the interaction terms. We find that when $|\mathbf{R}|$ is not too small, this formula is numerically better conditioned than the original, since the size of the integrand and the size of the integral is of the same order in $|\mathbf{R}|$, namely $1/|\mathbf{R}|^2$. For the original formulation, the cancellation of the $1/|\mathbf{R}|$ contributions in the integrand must be achieved numerically to give the $1/|\mathbf{R}|^2$ behavior of the integrand. In addition, the formula (17) includes the integrated force \mathbf{F}_k , instead of the force \mathbf{f}_k , reducing the order of the highest derivative of \mathbf{x}_k from four to three.

Similarly, integration by parts of $\mathbf{W}_k(\bar{\mathbf{x}})$ gives

$$\mathbf{W}_k(\bar{\mathbf{x}}) = - \int_{\Gamma_k} \frac{3(\hat{\mathbf{R}}_k \cdot (\mathbf{x}_k)_s)(\mathbf{I} - 5\hat{\mathbf{R}}_k\hat{\mathbf{R}}_k) + 3((\mathbf{x}_k)_s\hat{\mathbf{R}}_k + \hat{\mathbf{R}}_k(\mathbf{x}_k)_s)}{|\mathbf{R}_k|^4} \mathbf{F}_k(s') ds', \quad (18)$$

which shows explicitly its $1/|\mathbf{R}|^4$ decay.

The numerical computation of $\mathbf{V}_k(\bar{\mathbf{x}})$ and $\mathbf{W}_k(\bar{\mathbf{x}})$ is discussed in Section 3.

2.6. Periodicity

In a background shear flow, filaments in any random initial configuration get dispersed in the streamwise direction, and interactions are weak. It is therefore of interest to introduce periodic boundary conditions to keep filaments within smaller distances to each other, and thereby also better mimic an infinite domain with many interacting filaments.

In a grid based method, one simply imposes periodic boundary conditions to introduce periodicity into the problem. To do the same in this integral formulation, the sum in Eq. (6) needs to be extended to include

the contributions of all the periodic images of all filaments. Assume that the domain is periodic in the $\hat{\mathbf{e}}_j$ direction, and that the periodic length is d_j . Then, the sum in Eq. (6) becomes

$$\Pi_l^{\text{per}}(s) = \sum_{k=1}^M \sum_{p, p \neq 0} p \neq 0_{\text{for } k=l} \left[\mathbf{V}_k^p(\mathbf{x}_l(s)) + \frac{\varepsilon^2}{2} \mathbf{W}_k^p(\mathbf{x}_l(s)) \right], \quad (19)$$

where $\mathbf{V}_k^p(\bar{\mathbf{x}})$ is defined as $\mathbf{V}_k(\bar{\mathbf{x}})$ in Eq. (17), with \mathbf{R}_k replaced by $\mathbf{R}_k^p(s') = \bar{\mathbf{x}} - \mathbf{x}_k(s') + pd_j\hat{\mathbf{e}}_j$. Note that $\mathbf{V}_k^0(\bar{\mathbf{x}}) = \mathbf{V}_k(\bar{\mathbf{x}})$. Similarly, $\mathbf{W}_k^p(\bar{\mathbf{x}})$ is defined as $\mathbf{W}_k(\bar{\mathbf{x}})$ in (18) with $\mathbf{R}_k(s')$ replaced by $\mathbf{R}_k^p(s')$. The extension to more periodic directions is straightforward.

We can write the sum over p as

$$(1 - \delta_{kl})\mathbf{V}_k^0(\mathbf{x}_l(s)) + \sum_{p=1}^{\infty} [\mathbf{V}_k^{-p}(\mathbf{x}_l(s)) + \mathbf{V}_k^p(\mathbf{x}_l(s))].$$

For large p , one can show that $|\mathbf{V}_k^{-p}(\mathbf{x}_l(s)) + \mathbf{V}_k^p(\mathbf{x}_l(s))| \sim (pd_j)^{-3}$, i.e. we have a $1/|\mathbf{R}|^3$ decay of the terms in the periodic sum above. The terms $\mathbf{W}_k^p(\bar{\mathbf{x}})$ decay two orders faster in $1/|\mathbf{R}|$, and being multiplied by $\varepsilon^2/2$, they are negligible when $|\mathbf{R}|$ is not small.

Given this decay, we note that the sum above is unconditionally convergent. We discuss our numerical treatment of this sum in Section 3.4.

2.7. Problem summary

We now summarize the equations that the numerical algorithm will be based on. All equations are in non-dimensionalized form.

2.7.1. Single filament

Using the definition of the force in Eq. (9), the equation for the velocity of the filament centerline (2) in the case of one single filament can be written as

$$\bar{\mu}\mathbf{x}_t = \bar{\mu}\mathbf{U}_0 - \Lambda(s) \left[-(T\mathbf{x}_s)_s + \mathbf{x}_{ssss} \right] - \mathbf{K}_\delta \left[-(T\mathbf{x}_s)_s + \mathbf{x}_{ssss} \right]. \quad (20)$$

The boundary conditions for the free ends are $\mathbf{x}_{ss} = \mathbf{x}_{sss} = 0$ for $s = 0, 1$. The local operator Λ was defined in Eq. (3), and $\Lambda[-(T\mathbf{x}_s)_s + \mathbf{x}_{ssss}]$ can be explicitly expanded as

$$\Lambda[-(T\mathbf{x}_s)_s + \mathbf{x}_{ssss}] = 2cT_s\mathbf{x}_s + (c-2)T\mathbf{x}_{ss} - (c-2)\mathbf{x}_{ssss} - (c+2)(\mathbf{x}_s \cdot \mathbf{x}_{ssss})\mathbf{x}_s. \quad (21)$$

The auxiliary integro-differential equation for the line tension $T(s)$ in the case of one single filament is given by

$$\begin{aligned} 2cT_{ss} + (2-c)T(\mathbf{x}_{ss} \cdot \mathbf{x}_{ss}) - \mathbf{x}_s \cdot \frac{\partial}{\partial s} \mathbf{K}_\delta [(T\mathbf{x}_s)_s] &= \bar{\mu}\mathbf{x}_s \cdot \frac{\partial}{\partial s} \mathbf{U}_0 + (2-7c)(\mathbf{x}_{ss} \cdot \mathbf{x}_{ssss}) - 6c(\mathbf{x}_{ssss} \cdot \mathbf{x}_{ssss}) \\ &\quad - \mathbf{x}_s \cdot \frac{\partial}{\partial s} \mathbf{K}_\delta [\mathbf{x}_{ssss}] - \bar{\mu}\beta(1 - \mathbf{x}_s \cdot \mathbf{x}_s), \end{aligned} \quad (22)$$

which we write as

$$L_s[T, \mathbf{x}] = J[\mathbf{x}, \mathbf{U}_0], \quad (23)$$

together with the boundary condition $T = 0$ at $s = 0, 1$. $\beta \geq 0$ is the penalization parameter. The constant $c = \log(e^2e)$ and the non-dimensional constant $\bar{\mu} = 8\pi\mu\dot{\gamma}L^4/E$, as defined in Eq. (10).

The integral operator $\mathbf{K}_\delta[\mathbf{f}]$ is defined as

$$\mathbf{K}_\delta[\mathbf{f}](s) = \int_0^1 \left(\frac{\mathbf{I} + \hat{\mathbf{R}}(s, s')\hat{\mathbf{R}}(s, s')}{\sqrt{|\hat{\mathbf{R}}(s, s')|^2 + \delta(s)^2}} \mathbf{f}(s') - \frac{\mathbf{I} + \hat{\mathbf{s}}(s)\hat{\mathbf{s}}(s)}{\sqrt{|s - s'|^2 + \delta(s)^2}} \mathbf{f}(s) \right) ds', \quad (24)$$

where $\delta(s) = \delta_0\phi(s)$, where $\phi(s)$ is such that $\phi(s)/s$ and $\phi(s)/(1-s)$ are uniformly bounded. This regularization was introduced in Section 2.4, and our choice of $\phi(s)$ was given in Eq. (16). A detailed analysis is given in Appendix B.

2.7.2. Multiple filaments

For several filaments, we again index the filaments. For filament Γ_l , $l = 1, \dots, M$, the evolution equation is given by

$$\bar{\mu} \frac{\partial \mathbf{x}_l(s, t)}{\partial t} = \bar{\mu} \mathbf{U}_0(\mathbf{x}_l(s, t), t) - A[\mathbf{f}_l](s) - \mathbf{K}_\delta[\mathbf{f}_l](s) - \sum_{k=1, k \neq l}^M \left[\mathbf{V}_k(\mathbf{x}_l(s)) + \frac{\varepsilon^2}{2} \mathbf{W}_k(\mathbf{x}_l(s)) \right], \quad (25)$$

where $\mathbf{f}_l = -(T_l(\mathbf{x}_l)_s)_s + (\mathbf{x}_l)_{ssss}$. The expansion in Eq. (21) is used for evaluation of the local operator. The sum over the contribution from all other filaments to the velocity at filament l is replaced by $\Pi_l^{\text{per}}(s)$ in Eq. (19) in case of periodicity. The integrals $\mathbf{V}_k(\bar{\mathbf{x}})$ and $\mathbf{W}_k(\bar{\mathbf{x}})$ in Eqs. (17) and (18) contain the integrated force $\mathbf{F}_k = -T_k(\mathbf{x}_k)_s + (\mathbf{x}_k)_{sss}$.

The line tension equation for $T_l(s)$ in the case of several filaments reads like Eq. (22), with the subscript index l added, and with the addition of the following term to the right-hand side:

$$-(\mathbf{x}_l)_s \cdot \frac{\partial}{\partial s} \sum_{k=1, k \neq l}^M \left[\mathbf{V}_k(\mathbf{x}_l(s)) + \frac{\varepsilon^2}{2} \mathbf{W}_k(\mathbf{x}_l(s)) \right] = - \sum_{k=1, k \neq l}^M \Phi[T_k, \mathbf{x}_k, \mathbf{x}_l], \quad (26)$$

where the notation indicates that the integral terms in the sum depend on both T_k and \mathbf{x}_k through the integrated force \mathbf{F}_k . For $l = 1, \dots, M$, the line tension equation is given by

$$L_s[T_l, \mathbf{x}_l] = J[\mathbf{x}_l, \mathbf{U}_0] - \sum_{k=1, k \neq l}^M \Phi[T_k, \mathbf{x}_k, \mathbf{x}_l], \quad (27)$$

where we have used the notation in Eq. (23). Again, in case of periodicity, the first sum in expression (26) will be replaced by $\Pi_l^{\text{per}}(s)$ in Eq. (19), and the sum over Φ will be extended accordingly.

3. Numerical methods

In this section, we first discuss the numerical discretization for one single filament, and then extend to several interacting filaments.

The equations are discretized using a second-order time-stepping scheme, and second-order divided differences to discretize the spatial derivatives. Product integration is applied to the integral terms.

An explicit treatment of all terms in the time-dependent equation (20) would yield a very strict fourth-order stability limit for the time-step size, arising from the high derivatives of \mathbf{x} . To avoid this, we treat all occurrences of \mathbf{x}_{ssss} implicitly. We use a second-order backward differentiation formula [1]. Schematically, we write

$$\mathbf{x}_t = \mathbf{F}(\mathbf{x}, \mathbf{x}_{ssss}) + \mathbf{G}(\mathbf{x}), \quad (28)$$

where the dependence on \mathbf{x}_{ssss} is to be treated implicitly, and all other terms are to be treated explicitly. We approximate this decomposition by

$$\frac{1}{2\Delta t} (3\mathbf{x}^{n+1} - 4\mathbf{x}^n + \mathbf{x}^{n-1}) = \mathbf{F}(2\mathbf{x}^n - \mathbf{x}^{n-1}, \mathbf{x}_{ssss}^{n+1}) + 2\mathbf{G}(\mathbf{x}^n) - \mathbf{G}(\mathbf{x}^{n-1}), \quad (29)$$

where Δt is the time step, and $t^n = n\Delta t$. For example, as given by the notation for \mathbf{F} above, the nonlinear term $(\mathbf{x}_s \cdot \mathbf{x}_{ssss})\mathbf{x}_s$ in the local operator (21) is discretized as $((2\mathbf{x}_s^n - \mathbf{x}_s^{n-1}) \cdot \mathbf{x}_{ssss}^{n+1})(2\mathbf{x}_s^n - \mathbf{x}_s^{n-1})$. Combined with the spatial discretization that is described in the following, we find that this time discretization yields only a first-order constraint for the time-step size, i.e. Δt can be chosen proportional to the spatial grid size. For the very first time step, before any previous time levels are available, we replace the time discretization above by a first-order backward/forward Euler step.

Consider a uniform discretization in the arclength s of the filament centerline, with N intervals of step size $h = 1/N$. The discrete points are denoted $s_j = jh$, $j = 0, \dots, N$, and the values $f_j = f(s_j)$. Second-order divided differences are used to approximate spatial derivatives. D_p denotes divided difference operators such that $D_p f_j$ approximates $f^{(p)}(s_j)$ to an $O(h^2)$ error. Standard centered operators are used whenever possible, but at boundaries skew operators are applied. For exact definitions, see (A.1)–(A.4) in Appendix A. These stencils are used to compute \mathbf{x}_s , \mathbf{x}_{ss} , \mathbf{x}_{sss} and \mathbf{x}_{ssss} whenever needed. To apply the boundary conditions $\mathbf{x}_{ss} = \mathbf{x}_{sss} = 0$ for Eq. (20) at $s = 0$ and 1, one-sided stencils are used (as defined in (A.2) and (A.3)).

3.1. Product integration

When the integral operator \mathbf{K} was introduced in Eq. (4), we noted that the two terms in the integrand are both singular at $s' = s$, and that the integral is only well defined for the difference of these two terms. For the regularized operator, the terms are still nearly singular, and the numerical scheme must be designed with care to accurately treat the difference of these terms.

To evaluate the integral operator acting on \mathbf{x}_{ssss} , it is approximated by a piecewise linear polynomial

$$Q_1 \mathbf{x}_{ssss}(s) = D_4 \mathbf{x}_j + \frac{1}{h}(s - s_j)(D_4 \mathbf{x}_{j+1} - D_4 \mathbf{x}_j)$$

for $s_j \leq s \leq s_{j+1}$, for $j = 0, \dots, N - 1$. Here, D_4 is the second-order divided difference approximation to the fourth derivative, as defined in Eq. (A.4). Similarly, all other arguments to the integral operator \mathbf{K}_δ in Eqs. (20) and (22) are approximated as piecewise linear polynomials. The only exception is in the equation for the line tension (22), where $T(s)$ is approximated as a piecewise quadratic polynomial, so that its derivative $T_s(s)$ is a piecewise linear polynomial. That is,

$$Q_2 T(s) = T_j + \frac{1}{h}(s - s_j)(T_{j+1} - T_j) + \frac{1}{h^2}(s - s_j)(s - s_{j+1})(T_{j+1} - 2T_j + T_{j-1})$$

for $s_j \leq s \leq s_{j+1}$, for $j = 1, \dots, N - 1$. From the boundary conditions we have $T_0 = T_N = 0$. On the interval $[0, h]$, this formula is applied asymmetrically and involves T_0, T_1, T_2 .

We rewrite the integral operator (24) as

$$\begin{aligned} \mathbf{K}_\delta[\mathbf{g}](s) &= \int_0^1 \left[\frac{\mathbf{I} + \hat{\mathbf{R}}\hat{\mathbf{R}}}{\sqrt{|\hat{\mathbf{R}}|^2 + \delta(s)^2}} - \frac{\mathbf{I} + \hat{\mathbf{s}}\hat{\mathbf{s}}}{\sqrt{(s - s')^2 + \delta(s)^2}} \right] \mathbf{g}(s') ds' \\ &+ (\mathbf{I} + \hat{\mathbf{s}}\hat{\mathbf{s}}) \int_0^1 \frac{\mathbf{g}(s') - \mathbf{g}(s)}{\sqrt{(s - s')^2 + \delta(s)^2}} ds' = I_1(s) + I_2(s). \end{aligned} \quad (30)$$

Consider first $I_1(s)$, whose integrand vanishes for a straight filament. For part of this integrand, with $\delta = 0$ and s' close to s , Taylor series expansion yields

$$\frac{\hat{\mathbf{R}}\hat{\mathbf{R}}}{|\mathbf{R}|} - \frac{\hat{\mathbf{s}}\hat{\mathbf{s}}}{|s' - s|} = \text{sign}(s' - s)\mathbf{x}_s\mathbf{x}_{ss} + \mathbf{O}(s - s'),$$

and so, there is a jump discontinuity in the kernel. For $\delta > 0$, $\text{sign}(s' - s)$ is regularized as $\text{sign}(s' - s) \sim (s' - s)/\sqrt{(s' - s)^2 + \delta(s)^2}$, which is still a sharp transition for a small $\delta(s)$. Therefore, care must be taken when evaluating this integral.

We rewrite $I_1(s)$ as

$$I_1(s) = \int_0^1 \frac{\mathbf{G}(s, s')\mathbf{g}(s')}{\sqrt{(s - s')^2 + \delta(s)^2}} ds' \quad (31)$$

where $\mathbf{G}(s, s')$ is given by

$$\mathbf{G}(s, s') = \sqrt{\frac{(s - s')^2 + \delta(s)^2}{|\mathbf{R}|^2 + \delta(s)^2}}(\mathbf{I} + \hat{\mathbf{R}}\hat{\mathbf{R}}) - (\mathbf{I} + \hat{\mathbf{s}}\hat{\mathbf{s}}). \quad (32)$$

$\mathbf{G}(s, s')$ is a smooth function, that is $\mathbf{O}(s' - s)$ for s' close to s , and identically zero for a straight filament. Therefore, each component of \mathbf{G} can be approximated to second-order by a piecewise linear polynomial.

With both $\mathbf{G}(s, s')$ and $\mathbf{g}(s)$ piecewise polynomials, in order to evaluate both $I_1(s)$ and $I_2(s)$ we need to evaluate integrals of the form

$$\int_{s_j}^{s_{j+1}} \frac{(s' - s_j)^p}{\sqrt{|s - s'|^2 + \delta(s)^2}} ds' = \int_{s_j}^{s_{j+1}} \frac{(s' - s_j)^p}{\sqrt{(s' - s_j)^2 + b(s' - s_j) + c + \delta(s)^2}} ds' = \int_0^h \frac{\alpha^p}{\sqrt{\alpha^2 + b\alpha + c + \delta(s)^2}} d\alpha$$

where $b = 2(s_j - s)$ and $c = (s_j - s)^2$, and $p = 0, \dots, 4$. These integrals have analytical formulas, becoming somewhat lengthy as p increases. By evaluating these integrals analytically, the rapidly changing part where s' is close to s can be treated exactly. The highest polynomial degree ($p = 4$) is needed for the term $T\mathbf{x}_{ss}$ in the line tension equation, where T is piecewise quadratic and \mathbf{x}_{ss} is piecewise linear. This results in a cubic $\mathbf{g}(s)$ in the notation above, to be multiplied by $\mathbf{G}(s, s')$ in the evaluation of $I_1(s)$.

3.2. Discretization of the line tension equation

In the line tension equation (22), terms like $\mathbf{x}_s \cdot (\partial/\partial s)\mathbf{K}_\delta[\mathbf{g}]$ appear. These differentiated integral terms are approximated to second order by

$$\frac{\partial}{\partial s}\mathbf{K}_\delta[\mathbf{g}](s)|_{s=s_i} \approx \frac{1}{h} [\mathbf{K}_\delta[\mathbf{g}](s_{j+1/2}) - \mathbf{K}_\delta[\mathbf{g}](s_{j-1/2})]. \quad (33)$$

For each half point $s_{j+1/2}$, the values of all terms in the integral operator that are functions of s are computed by linear interpolation using the values at s_j and s_{j+1} . The integral over s' is then evaluated as usual. The compact centered approximation of the derivative in Eq. (33) is important to achieve a stable numerical approximation of the line tension equation.

From the second part of the integral operator $I_2(s)$ in Eq. (30), $\mathbf{x}_s \cdot (\partial/\partial s)\mathbf{K}_\delta[\mathbf{g}]$ (with $\mathbf{g}(s) = (T\mathbf{x}_s)_s$ and \mathbf{x}_{ssss}), yields a term

$$\mathbf{x}_s \cdot \frac{\partial}{\partial s} [I_2(s)] = \mathbf{x}_s \cdot \frac{\partial}{\partial s} \left[(\mathbf{I} + \hat{\mathbf{s}}\hat{\mathbf{s}}) \int_0^1 \frac{\mathbf{g}(s') - \mathbf{g}(s)}{\sqrt{(s-s')^2 + \delta(s)^2}} ds' \right]. \quad (34)$$

There are several factors to consider when deciding how to numerically discretize this expression. It is important to achieve a good cancellation between the two terms in the integral operator in Eq. (34), which vary rapidly close to the boundary. It is especially important since we are taking a derivative of the result.

There are also some considerations for the interior errors. The second term of $\mathbf{x}_s \cdot (\partial/\partial s)(I_2(s))$ in Eq. (34) is $-\mathbf{x}_s \cdot (\partial/\partial s)[(\mathbf{I} + \hat{\mathbf{s}}\hat{\mathbf{s}})\mathbf{g}(s)\varphi(s)]$, where

$$\varphi(s) = \log(\delta(s)^{-2} \left(1 - s + \sqrt{(1-s)^2 + \delta(s)^2} \right) \left(s + \sqrt{s^2 + \delta(s)^2} \right)). \quad (35)$$

Carrying out the differentiation, this yields a term in which $\mathbf{g}(s)$ is differentiated. For $\mathbf{g}(s) = \mathbf{x}_{ssss}$, this will yield \mathbf{x}_{sssss} .

The best treatment in order to reduce the errors in the interior is to analytically reformulate terms with higher derivatives. We can use the ladder of identities in expression (12), extended by

$$\mathbf{x}_s \cdot \mathbf{x}_{sssss} = -3\mathbf{x}_{sss} \cdot \mathbf{x}_{sss} - 4\mathbf{x}_{ss} \cdot \mathbf{x}_{ssss}, \quad (36)$$

to express select higher order terms as lower order ones.

In doing this, we will however treat differently the two terms in Eq. (34), and the cancellation between the two close to the boundary, where the terms vary rapidly, will not be as good. Indeed, there is a trade off between achieving good boundary treatment and the smallest possible interior errors. Introducing a constant $\varphi_0 \neq 0$, we can write $\tilde{\mathbf{g}}(s)\varphi(s) = \tilde{\mathbf{g}}(s)[\varphi(s) - \varphi_0] + \tilde{\mathbf{g}}(s)\varphi_0$. With $\varphi_0 = \varphi(1/2)$ (Eq. (35)), the bulk of the total term is in the second part in the interior, while the rapid transition at the boundaries occurs in the first part.

In this manner we split the second term of the integral into two terms – one term which we add to the first term of the integral before applying $\frac{\partial}{\partial s}$, and a second term which is reformulated analytically. In this way, the bulk of the total term will be reformulated analytically, reducing the interior errors, while the boundary treatment is unaffected.

Following these ideas, the quadrature has been implemented the following way. For $\mathbf{g}(s) = (T\mathbf{x}_s)_s$, we rewrite Eq. (34) as

$$\begin{aligned} & \mathbf{x}_s \cdot \frac{\partial}{\partial s} \left[(\mathbf{I} + \hat{\mathbf{s}}\hat{\mathbf{s}}) \int_0^L \frac{(T\mathbf{x}_s)_s(s') - (T\mathbf{x}_s)_s(s)}{\sqrt{(s-s')^2 + \delta(s)^2}} ds' \right] \\ &= \mathbf{x}_s \cdot \frac{\partial}{\partial s} \left[(\mathbf{I} + \hat{\mathbf{s}}\hat{\mathbf{s}}) \left(\int_0^1 \frac{(T\mathbf{x}_s)_s(s') - (T\mathbf{x}_s)_s(s)}{\sqrt{(s-s')^2 + \delta(s)^2}} ds' + \varphi_0(T\mathbf{x}_s)_s(s) \right) \right] - (2T_{ss} - T(\mathbf{x}_{ss} \cdot \mathbf{x}_{ss}))\varphi_0 \end{aligned} \quad (37)$$

with $\varphi_0 = \varphi(1/2)$, as defined in Eq. (35). To improve the numerical treatment of the integral with $\mathbf{g}(s) = \mathbf{x}_{ssss}$, we rearrange and reformulate it as

$$\begin{aligned}
& \mathbf{x}_s \cdot \frac{\partial}{\partial s} \left[(\mathbf{I} + \hat{\mathbf{S}}\hat{\mathbf{S}}) \int_0^L \frac{\mathbf{x}_{ssss}(s') - \mathbf{x}_{ssss}(s)}{\sqrt{(s-s')^2 + \delta(s)^2}} ds' \right] \\
&= -6 \frac{\partial}{\partial s} \left[\int_0^L \frac{\mathbf{x}_{ss}(s') \cdot \mathbf{x}_{sss}(s') - \mathbf{x}_{ss}(s) \cdot \mathbf{x}_{sss}(s)}{\sqrt{(s'-s)^2 + \delta(s)^2}} ds' + \varphi_0 \mathbf{x}_{ss}(s) \cdot \mathbf{x}_{sss}(s) \right] \\
&\quad - 2 \frac{\partial}{\partial s} \left[\int_0^L \frac{\mathbf{x}_{ssss}(s') \cdot (\mathbf{x}_s(s') - \mathbf{x}_s(s))}{\sqrt{(s'-s)^2 + \delta(s)^2}} ds' \right] \\
&\quad + \mathbf{x}_{ss} \cdot \int_0^L \frac{\mathbf{x}_{ssss}(s') - \mathbf{x}_{ssss}(s)}{\sqrt{(s'-s)^2 + \delta(s)^2}} ds' + 6\varphi_0 (\mathbf{x}_{ss} \cdot \mathbf{x}_{ssss} + \mathbf{x}_{sss} \cdot \mathbf{x}_{sss}). \tag{38}
\end{aligned}$$

In this way, there are in effect no \mathbf{x}_{ssss} terms computed, as was the case in the original formulation. The $\partial/\partial s$ operator is discretized with a centered narrow approximation as given in Eq. (33).

3.3. Numerical methods for several filaments

The dynamics of multiple filaments are coupled to each other through the sum in Eq. (25). In this section, we discuss both the temporal and spatial treatments of this term.

3.3.1. Time-stepping

The evolution of the centerline of one filament is coupled to the evolution of all others, through the sum in Eq. (25). We treat this coupling term explicitly (that is, as part of $\mathbf{G}(\mathbf{x})$ in (29)) in our time integration scheme). That means that in the dynamics of $\mathbf{x}_l(s, t)$, $l = 1, \dots, M$, only $(\mathbf{x}_l)_{ssss}$ is treated implicitly. In the resulting linear system for $\mathbf{x}_l^{n+1}(s)$, $l = 1, \dots, M$, the contribution from the other filaments will therefore be in the right-hand side, and so the big system decouples into separate linear systems for $\mathbf{x}_l^{n+1}(s)$, $l = 1, \dots, M$.

In the coupling term, the derivatives $(\mathbf{x}_k)_{sss}$ for $k \neq l$ appear through the integrated force $\mathbf{F}_k(s)$ in the integrals \mathbf{V}_k and \mathbf{W}_k in Eqs. (17) and (18). These integrals can be considered as smoothing operators on $(\mathbf{x}_k)_{sss}$ so long as the filaments remain well separated. We find in most instances that the explicit treatment of this term as done does not alter the first-order time-stepping constraint that holds for the discretized problem for one single filament.

3.3.2. Solving for the tensions

The equation for the line tensions $T_l(s)$, $l = 1, \dots, M$, is given in (27). This is a system of coupled time-independent integro-differential equations that, given certain shapes of the filaments, yields the corresponding line tensions. To avoid solving one very large linear system for the line tensions on all the filaments, we introduce a fixed point iteration, in which we use the newest updates of the T_k 's available ($k \neq l$), when computing $T_l(s)$.

Introducing an iteration index q , we initialize T_l^0 , $l = 1, \dots, M$, to be the line tensions corresponding to the filament shapes at the previous time steps. In iteration $q \geq 1$, for $l = 1, \dots, M$, solve

$$L_s[T_l^q, \mathbf{x}_l] = J[\mathbf{x}_l, \mathbf{U}_0] - \sum_{k=1}^{l-1} \Phi[T_k^q, \mathbf{x}_k, \mathbf{x}_l] - \sum_{k=l+1}^M \Phi[T_k^{q-1}, \mathbf{x}_k, \mathbf{x}_l] \tag{39}$$

for T_l^q and define ϱ_l^q to be the relative max norm of the difference between consecutive iterates T_l^q and T_l^{q-1} . Set $\varrho^q = \max_l \varrho_l^q$. The iteration is terminated when ϱ^q is below a given tolerance.

3.3.3. Spatial evaluation

To evaluate the integrals $\mathbf{V}_k(\mathbf{x}_l(s))$ and $\mathbf{W}_k(\mathbf{x}_l(s))$ in the sum in Eq. (6) we use the trapezoidal rule. This is a second-order method and it is accurate so long as $|\mathbf{R}|$ is not too small.

When evaluating these integrals it might occur that two filaments come within close proximity of each other. If, for a fixed s value on filament l , $|\mathbf{R}| < 12h$ for any node value of s' on filament k , we perform a refined calculation of the integral. There are two levels of refinement. The first is to simply divide the intervals in the integral where \mathbf{R} is small into five subintervals, and use the trapezoidal rule on each of these. This yields a better approximation of the $1/|\mathbf{R}|^2$ and $1/|\mathbf{R}|^4$ terms. The second refinement level is needed when we get within an ε -scale from the filament centerline.

To compute the velocity contribution from a filament, there are two different formulas available. Away from filament k , we compute the velocity contribution at a point $\bar{\mathbf{x}}$ from this filament by evaluating $\mathbf{V}_k(\bar{\mathbf{x}}) + (\varepsilon^2/2)\mathbf{W}_k(\bar{\mathbf{x}})$. If $\bar{\mathbf{x}}$ would fall on the centerline of filament k , the velocity modification that this filament introduces can be computed using the right-hand side of the time-dependent equation (20), with $\mathbf{U}_0 = 0$.

The first formula is not defined as the distance to the centerline goes to zero. The second formula is valid within the filament; in the derivation it was assumed that the velocity on the surface of the filament is a function of s only, without any angular dependence. These formulas differ slightly on the surface of the filament, see the discussion after Eq. (5).

Assuming that the radius of the filament is uniformly ε (even though the filaments are actually tapered), two centerlines of different filaments should not be closer than 2ε apart, and if they touch, they should move with the same velocity at that point. Denoting the normal distance to the filament centerline by d , it is therefore natural to set the velocity to the centerline velocity if $d \leq d_0$, interpolate linearly between the two approximations if $d_0 < d < 2d_0$, and use the regular velocity formula if $d \geq 2d_0$. The natural choice would be $d_0 = 2\varepsilon$, which we for our discretization modify to read $d_0 = \max(h, 2\varepsilon)$, where h is the grid size in the arclength s .

3.4. Imposing periodicity

The introduction of periodicity to the problem was discussed in Section 2.6, where the sum $\Pi_l^{\text{per}}(s)$ was introduced. This sum includes not only the velocity contributions from all the other filaments, but from all the periodic images.

Assume that we want to compute the contribution from filament k to filament l . In the case of periodicity, for $i = 0, \dots, N$, we need to compute

$$\sum_{\substack{p=-\infty, \\ p \neq 0 \text{ for } k=l}}^{\infty} \left[\mathbf{V}_k^p(\mathbf{x}_l(s_i)) + \frac{\varepsilon^2}{2} \mathbf{W}_k^p(\mathbf{x}_l(s_i)) \right]. \quad (40)$$

The \mathbf{R} -vector in the definitions of \mathbf{V}_k^p and \mathbf{W}_k^p is then given by $\mathbf{R}_k^p(s') = \mathbf{x}_l(s_i) - \mathbf{x}_k(s') + pd_j \hat{\mathbf{e}}_j$; see the remark below Eq. (19).

The second term, $\mathbf{W}_k^p(\mathbf{x}_l(s_i))$, is multiplied by $\varepsilon^2/2$ and decays as $1/|\mathbf{R}_k^p|^4$. It is therefore negligible for all but small $|\mathbf{R}_k^p|$.

As $|p|$ is increased, i.e. as $|\mathbf{R}_k^p|$ gets large, $\mathbf{R}_k^p(s')$ will not vary much in the integrand for $\mathbf{V}_k^p(\bar{\mathbf{x}})$. We make the approximation to replace $\mathbf{R}_k^p(s')$ with $\mathbf{R}_k^p(1/2)$ and move it out of the integral. We will then only need to integrate one symmetric dyadic product

$$\int_{\Gamma_k} (\mathbf{x}_k)_s \mathbf{F}_k(s') \, ds'. \quad (41)$$

Once we have the six independent components of this integral, and $\mathbf{R}^p(1/2)$ for any p , we can for any $\bar{\mathbf{x}}$ compute the approximation $\tilde{\mathbf{V}}_k^p(\bar{\mathbf{x}})$ to $\mathbf{V}_k^p(\bar{\mathbf{x}})$ as defined below the sum (19).

We now replace the sum (40) by

$$\sum_{\substack{p=-1, \\ p \neq 0 \text{ for } k=l}}^1 \left[\mathbf{V}_k^p(\mathbf{x}_l(s_i)) + \frac{\varepsilon^2}{2} \mathbf{W}_k^p(\mathbf{x}_l(s_i)) \right] + \sum_{2 \leq |p| \leq Q} \tilde{\mathbf{V}}_k^p(\mathbf{x}_l(s_i)), \quad (42)$$

where $\tilde{\mathbf{V}}_k^p(\bar{\mathbf{x}})$ is defined as $\mathbf{V}_k(\bar{\mathbf{x}})$ in (17), but with $\mathbf{R}_k(s')$ replaced by $\mathbf{R}_k^p(1/2)$.

In total, $2Q + 1$ terms are included in the sum. We compute the contributions from filament k and its two closest periodic images without any approximation. For the contributions from the images further away, we approximate $\mathbf{V}_k^p(\bar{\mathbf{x}})$ by $\tilde{\mathbf{V}}_k^p(\bar{\mathbf{x}})$, and neglect $\varepsilon^2 \mathbf{W}_k^p(\bar{\mathbf{x}})/2$. If $k = l$, the only difference is that the term $p = 0$ is excluded from the sum.

We have assumed here that $|\mathbf{R}_k^p(s')|$ is smallest for $p = 0$. The domain is however periodic, and it might as well instead be smallest for $p = -1$ or $p = 1$. If this is the case, the indexing of the summation should be shifted accordingly, so as to be centered around that p value.

In Appendix C, we present numerical results that show that adding the sum over the approximate terms in Eq. (42) is a substantial improvement compared to simply truncating the sum at $|p| = 1$.

For each filament, we only need to evaluate the integral (41) once, where after we can form the periodic contribution from this filament to any other filament by multiplying by constant terms and summing up. Therefore, this improvement can be done to a very small extra cost.

The approximate sum (42) is used also in the line tension equation, where we write $(\mathbf{x}_l)_s \cdot \partial/\partial s$ acting on this sum as

$$\sum_{\substack{p=-1, \\ p \neq 0 \text{ for } k=l}}^1 \Phi^p[T_k, \mathbf{x}_k, \mathbf{x}_l] + \sum_{2 \leq |p| \leq Q} \tilde{\Phi}^p[T_k, \mathbf{x}_k, \mathbf{x}_l] \quad (43)$$

in accordance with the notation introduced in Eq. (26).

3.5. Summary of the numerical algorithm

Assume that we are on time level t^n , and that \mathbf{x}_l^n and \mathbf{x}_l^{n-1} are known, for all filaments $l = 1, \dots, M$. To advance to time level $n + 1$, for each filament Γ_l , $l = 1, \dots, M$, do the following:

- (i) Compute first- to fourth-order spatial derivatives of \mathbf{x}_l^n using the difference stencils defined in Appendix A.
- (ii) Compute the line tension T_l^n . The line tension equation (22) is an auxiliary equation, and is a function of an instantaneous shape \mathbf{x} and the parameters of the problem only. In the case of several filaments, apply the fixed point iteration introduced in Eq. (39).
- (iii) Compute the contribution from all other filaments on the level n , the sum in Eq. (25), in the manner discussed in Section 3.3.
- (iv) To obtain \mathbf{x}_l^{n+1} , solve Eq. (25), with $\mathbf{f}_k = -(T_k(\mathbf{x}_k)_s)_s + (\mathbf{x}_k)_{ssss}$. In doing this, we use the time discretization (29), with all occurrences of $(\mathbf{x}_l)_{ssss}$ treated implicitly. All other terms defined on filament l , as well as the sum of the contributions from the other filaments are treated explicitly.

These are the main steps of the algorithm. Below follows some additional comments about the solution process.

- In the case of periodicity:
 - In (ii), replace the sum in Eq. (25) by $\Pi_l^{\text{per}}(s)$ in Eq. (19). Compute $\Pi_l^{\text{per},n}(s)$ by replacing each sum over p as in Eq. (40) by the approximate sum in Eq. (42).
 - In (iii), add the term for $k = l$ in the right sum in (39), and replace $\Phi[T_k, \mathbf{x}_k, \mathbf{x}_l]$ in the sums by the approximate periodic sum in (43).

- Through the fixed point iteration introduced for the line tension equation (Eq. (39)), the line tension solves on the different filaments are decoupled. On each filament we need to solve a linear system of equations for the node values $(T_i)_i$, $i = 1, \dots, N - 1$ ($T_0 = T_N = 0$ due to the boundary conditions). Due to the non-local integral operator in the left-hand side of Eq. (22), the matrix will be full, and we solve the system by direct LU factorization.
- Since the contribution from the other filaments is treated explicitly in the time-dependent equation (iv), also here we solve a system of equations for each filament, with the coupling terms in the right-hand side. The number of unknowns is $3(N + 1)$; the x , y and z coordinates for s_i , $i = 0, \dots, N$. Due to the implicit treatment of the non-local integral operator acting on $(\mathbf{x}_i)_{ssss}$, the system matrix is full. Again, we use a direct method to solve this system.

In addition to the physical parameters of the problem, we have introduced a few numerical parameters. In our simulations, if nothing else is noted, we define $\delta(s) = \delta_0 \phi(s)$ with $\phi(s)$ as in Eq. (16) with $\gamma = 0.1$ and $\delta_0 = 2\varepsilon$. The penalty parameter β in the line tension equation is typically set to 20. The time-step size Δt and N (where the grid size $h = 1/N$) will be given for each run. In case of periodicity, Q in the sum (42) is typically set to 20.

4. Numerical results

4.1. One single filament in the plane

A straight rod in a plane shear flow will rotate about its center and possibly translate with the fluid. However, a flexible rod can become unstable to buckling if the shear rate is high enough. We begin by giving the analytical solution assuming that the filament is perfectly straight, and then move to results for the general case.

Assume that a straight filament is inserted in the xy -plane in a planar shear flow $\mathbf{U}_0(\mathbf{x}) = \alpha(t)(y, 0, 0)$, with its center point at $(0, 0, 0)$. Let θ be the angle of the filament to the x -axis; see Fig. 1.

We then have the following exact solution to the unregularized slender body equations:

$$\mathbf{x}(s, t) = \frac{1}{2}(1 - 2s)\hat{\mathbf{e}}_\theta, \quad T(s) = -\frac{\bar{\mu}}{8} \frac{\alpha(t) \sin 2\theta}{c + 2} s(1 - s), \quad (44)$$

$s \in (0, 1)$, where $\hat{\mathbf{e}}_\theta = (\cos \theta, \sin \theta, 0)$ and $\theta(t)$ is given by

$$\theta_t = -\alpha(t) \sin^2 \theta, \quad \theta(0) = \theta_0. \quad (45)$$

In classical work, Jeffery provided the analogous exact solution for a long slender ellipsoid in a shear flow² [20]. The so-called ‘‘Jeffery orbit’’ for a constant shear flow ($\alpha(t) = 1$) is

$$\theta_t = \frac{-1}{1 + \varepsilon^2} (\sin^2 \theta + \varepsilon^2 \cos^2 \theta). \quad (46)$$

From this, one sees that there is an $O(\varepsilon^2)$ error in the angular velocity in the solution from the slender body equations (45). This is within the order of accuracy of the slender body approximations. However, in the special case of inserting the straight filament parallel to the x -axis, there will be no rotation in the slender body approximation. In reality, there will be a small torque acting on the filament in this case, and this $O(\varepsilon^2)$ contribution is disregarded in the slender body approximation, and captured in Eq. (46).

For a straight filament held fixed in a uniform flow in alignment with the flow, the slender body equations yield a drag coefficient of $2/3[\log(2/\varepsilon) - 1/2]^{-1}$, as normalized by half the filament length. If the

² The shape $r(s) = 2\varepsilon\sqrt{s(1-s)}$, assumed when deriving the slender body equations is that of a long slender ellipsoid.

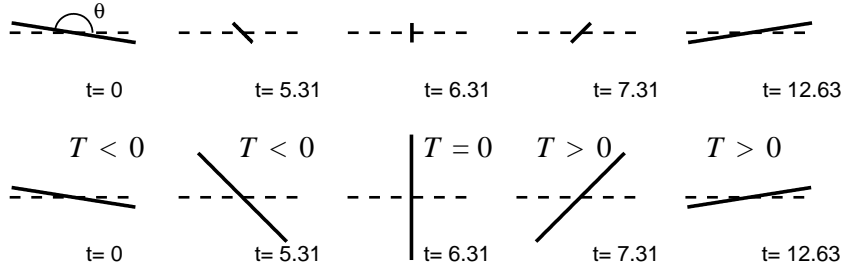


Fig. 1. Rotation of a straight filament with $U_0(\mathbf{x}(s)) = (y(s), 0)$. Upper row: without line tension ($T = 0$). Lower row: line tension $T(s)$ included.

filament orientation is orthogonal to the flow direction, the drag coefficient is $4/3[\log(2/\varepsilon) + 1/2]^{-1}$. These two results agree to $O(\varepsilon^2)$ to the exact result of Chang and Wu [7] for an ellipsoid, the base shape upon which our slender body theory is based 2, see [21].

The Jeffrey orbit solution yields that the time to complete one period is $T_{\text{period}} = 2\pi(\varepsilon^{-1} + \varepsilon)$. For a slender filament, only a small fraction of this time is needed to cover a majority of the orbit. The rest of the time is spent in alignment or near alignment with the x -axis. As ε decreases, the time needed to cover the main part of the orbit stays almost the same, while the period time increases linearly in ε^{-1} . Hence, for $\varepsilon = 10^{-2}$, it takes only about 4% of the period time to cover 90% of the orbit, for $\varepsilon = 10^{-3}$ it takes approximately 0.4% of the time, for $\varepsilon = 10^{-4}$, 0.04%, etc.

This simple case of a straight filament also offers insight into the action of the line tension. When the filament is inserted at an angle of θ_0 , the y -coordinates of the end points are $\sin \theta_0$, and $-\sin \theta_0$, respectively. Without any tension in the fiber, to resist compression and extension, the points on the filament will follow the background shear flow, and the filament will initially be compressed. At $\theta = \pi/2$, the length will be $2 \sin \theta_0$. After this point the filament will be extended again. When the line tension is included as given by the inextensibility condition, the filament rotates with a fixed length; see Fig. 1. The line tension is initially negative in order to resist the compression of the filament. When the filament becomes vertical, it is in a neutral position, and the line tension is zero. As the filament continues to rotate, it comes under extension, and the line tension becomes positive in order to prevent the filament to extend. The total velocity field $\mathbf{U}(\mathbf{x})$ that produces this motion differs significantly from the undisturbed shear flow $\mathbf{U}_0(\mathbf{x})$ in points close to the filament.

If we introduce a small perturbation to the inextensible filament, so that it is not exactly straight, then there are two possible scenarios. One is that this perturbation will disappear with time and the filament will become straight. However, if the filament is under compression for some time, and if the value of $\bar{\mu}$, which relates the strength of the shear flow to the bending rigidity of the filament, is large enough, then buckling occurs [4]. As we increase $\bar{\mu}$, this buckling becomes more pronounced. This is demonstrated in Figs. 2–4, where we display the results from simulations of a single, flexible filament.

The initial angle θ_0 is chosen such that a straight filament inserted at this angle at $t = 0$ will be vertical at $t = 49.664$. This yields $\theta_0 = \pi - \arcsin(\eta)$, where $\eta = (49.664^2 + 1)^{-1/2}$ and $\theta_0 \approx 0.9936\pi$. We define the initial shape as

$$\begin{aligned} x(\alpha) &= \cos(\theta_0)(\alpha - 1)/2, \\ y(\alpha) &= \sin(\theta_0)(\alpha - 1)/2 + d_y \alpha^4 (1 - \alpha)^4 \end{aligned} \quad (47)$$

for $\alpha \in (0, 1)$, with $d_y = -10^{-4}$. We then numerically rescale x and y as functions of the arclength s , such that the length of the filament is 1. This is a very small perturbation compared to a straight filament. The numerical parameters for the runs are $N = 200$, $\Delta t = 0.0064$. We have $\varepsilon = 10^{-3}$ and $\delta_0 = 2\varepsilon$.

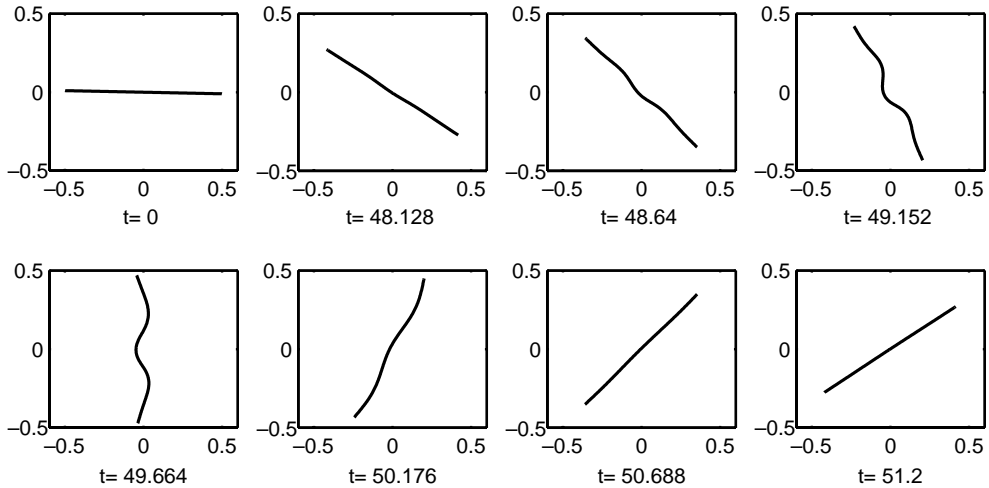


Fig. 2. Slight buckling occurs for $\bar{\mu} = 2 \times 10^5$.

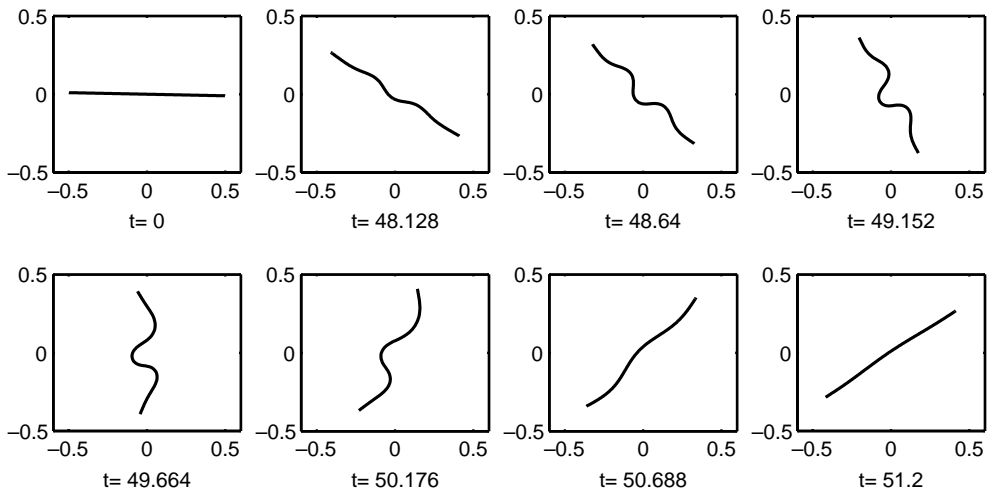


Fig. 3. Pronounced buckling occurs for $\bar{\mu} = 3 \times 10^5$.

We note that if the initial configuration \mathbf{x} is reflected to $-\mathbf{x}$, it will evolve under the symmetry $\mathbf{x} \rightarrow -\mathbf{x}$. Hence, if we change the sign of the perturbation, the filament will buckle in the other direction.

With the initial angle of the filament being somewhat smaller than 180° , it will slowly start to rotate. Until it has passed the vertical axis, it is under compression, most strongly when it is at 45° angle to the x -axis. As the vertical line is passed, the filament comes under extension. If a buckling occurs, it occurs while the filament is under compression, and the filament will later extend to a straight shape again. As $\bar{\mu}$ increases, the fluid can exert a greater and greater compressive stress on the filament, inducing a larger buckling.

In Fig. 5, the line tension $T(s)$ corresponding to the filament shapes in Fig. 3 has been plotted. The analytical solution for a straight filament (Eq. (44)) is plotted for comparison (dashed line). For a straight filament, the line tension is a negative parabolic function up to the time where the filament is vertical, to resist a compression of the filament. Also here, the line tension starts out similar to this, but as the filament

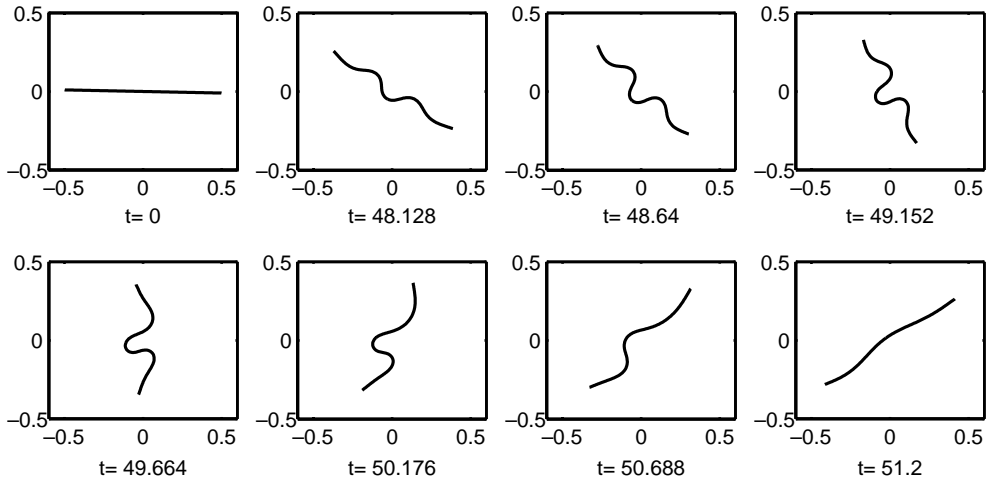


Fig. 4. Substantial buckling occurs for $\bar{\mu} = 4 \times 10^5$.

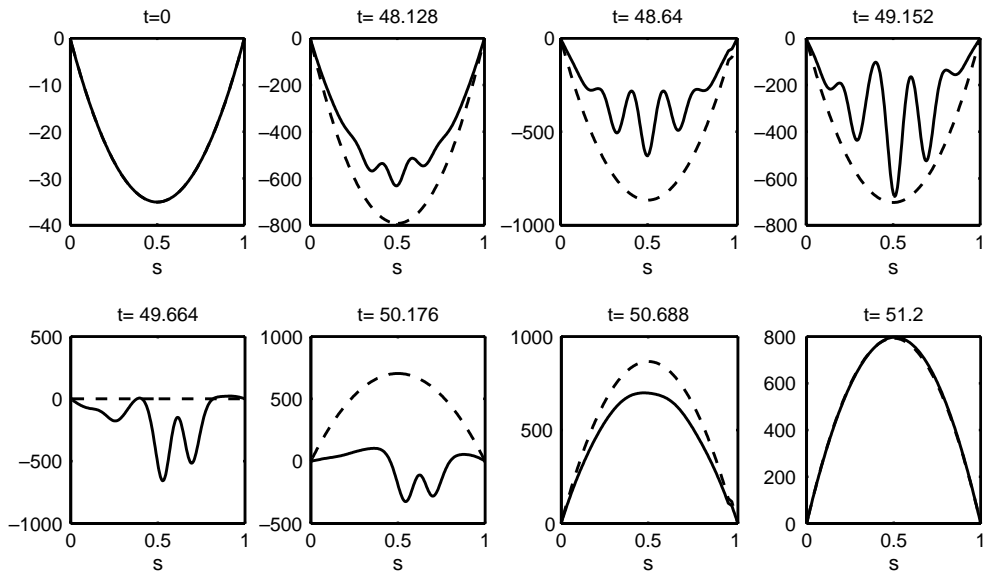


Fig. 5. The line tension $T(s)$ corresponding to the filament shapes in Fig. 3. The analytical solution for a straight filament (Eq. (44)) is plotted for comparison (dashed line).

buckles, is attained a more complicated structure, needed to enforce the inextensibility for this curved filament. When the filament extends to a straight shape again, the line tension attains once more its parabolic shape, with a positive sign to resist the extension.

The contribution of the fiber forces to the fluid stress (in addition to the stress tensor for the background flow) can be computed as

$$\Sigma = \int_0^1 \mathbf{f}(s)\mathbf{x}(s) ds, \tag{48}$$

where $\mathbf{f}\mathbf{x}$ is a dyadic product, see [3].

Since the stress tensor is only determined to within an additive isotropic tensor, only the normal stress differences $N_1 = \Sigma_{11} - \Sigma_{22}$ and $N_2 = \Sigma_{22} - \Sigma_{33}$ can be measured in experiments. For a linearly sheared Newtonian fluid (i.e. with no filaments present), the normal stress differences are zero. For a non-Newtonian fluid, the first normal stress difference can be measured in for example a cone-and-plate rheometer, as the thrust per unit area of the plate. This thrust tends to push the plates apart if N_1 is positive, but tends to pull them together if N_1 is negative.

The evolution of N_1 for a straight filament (dashed curve) and a buckling filament (solid curve) is shown in Fig. 6. As the straight filament rotates in a shear flow, the integrated normal stress difference over a full rotation is zero and hence does not yield a net contribution. (This is in generally true for a single straight rod, as can be shown by direct calculation). If the filament bends, this is not true. The symmetry of the first normal stress difference that holds for a straight filament is broken, and there is a net contribution. The integral over the time interval shown in Fig. 6 yields 0 for the straight filament (dashed line) but 579.3 for the buckling filament. The anti-symmetric configuration $\mathbf{x} \rightarrow -\mathbf{x}$ yields identical normal stresses, and hence there is no configuration that can yield a negative normal stress contribution that can cancel the positive contribution.

The extra stress tensor is symmetric, and the shear stress $\Sigma_{12} = \Sigma_{21}$ is plotted in Fig. 7. As a comparison, we plot with a dashed line the shear stress for a straight filament, and can note that the filament, by the buckling, reduces the added shear stress.

4.1.1. Convergence

To check the convergence of our numerical method, we have performed the same runs as presented in Figs. 2–4 with $N = 200$ also with $N = 50$ and $N = 100$ points. The time step is scaled accordingly, and so the three set of runs have been made with $(N, \Delta t) = (50, 0.0256)$, $(100, 0.0128)$ and $(200, 0.0064)$. Note the

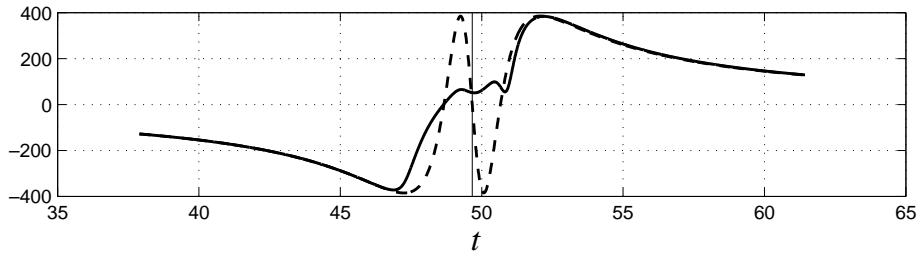


Fig. 6. The first normal stress difference $N_1 = \Sigma_{11} - \Sigma_{22}$ is plotted as a function of time, for $\bar{\mu} = 4 \times 10^5$. The normal stress difference for a straight filament, same $\bar{\mu}$ is plotted with a dashed line for comparison. The solid vertical line indicates $t = 49.664$, the time at which the straight filament is vertical.

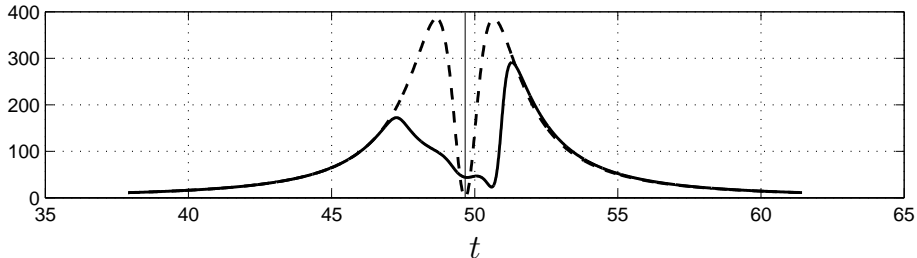


Fig. 7. The shear stress $\Sigma_{12} = \Sigma_{21}$ is plotted as a function of time, for $\bar{\mu} = 4 \times 10^5$. $\Sigma_{12} = \Sigma_{21}$ for a straight filament, same $\bar{\mu}$ is plotted with a dashed line for comparison.

absence of any high order time-step constraint. The largest differences between the three resolutions is naturally found in the simulations for the largest $\bar{\mu}$ -value, where the filament bends the most. For the times plotted in Fig. 4, the convergence rate based on the consecutive solutions varies between 1.89 and 2.22. The norm we use is the average error in the Euclidean distance between the discrete points on the filament. For the lower values of $\bar{\mu}$, $N = 50$ also resolved the filament shape well, as seen in the left plot of Fig. 8 for $\bar{\mu} = 3 \times 10^5$. However, when we increase $\bar{\mu}$, so that we get an even higher curvature of the filament, $N = 50$ is not a sufficient resolution, as seen in the right plot in Fig. 8 ($\bar{\mu} = 4 \times 10^5$). The errors are largest in the most bent region in the center of the filament, and also near the free ends.

The filament is inextensible, so it is also of interest to monitor the length errors during the simulations. The error in the length of the filament is naturally largest when the filament is most buckled. In Fig. 9, the absolute values of the length errors as a function of time have been plotted for the three sets of runs. From left to right we have $\bar{\mu} = 2 \times 10^5$, 3×10^5 and 4×10^5 , and in each plot, the length error is plotted for $N = 50$, 100 and 200. In all three sets of runs, the peak in the length error is reduced by more than a factor of four as the resolution is doubled. We have used the penalization in the line tension equation as introduced in Eq. (22), with $\beta = 20$.

Without penalization, the length errors would be larger, and could render very inaccurate simulations for cases with large deformations. The exact choice of β is however not so important: choices of $\beta = 10$, 20 or 50 affect the results only very marginally.

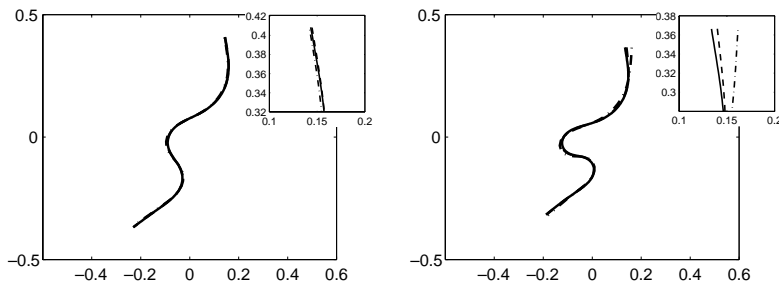


Fig. 8. Comparison at $t = 50.176$ between solutions from run with $N = 50$ (dash-dot), $N = 100$ (dashed) and $N = 200$ (solid). In the left plot, $\bar{\mu} = 3 \times 10^5$, as in Fig. 3 and in the right plot $\bar{\mu} = 4 \times 10^5$, as in Fig. 4. The convergence rates p based on consecutive solutions are 1.98 and 1.90, respectively.

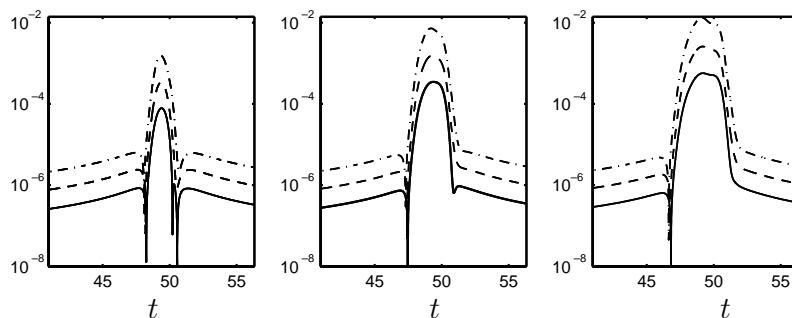


Fig. 9. The length errors versus time t for runs with $\varepsilon = 1e - 3$ and $\bar{\mu} = 2 \times 10^5$, 3×10^5 and 4×10^5 , from left to right. The length errors have been plotted for the different resolutions $N = 50$ (dash-dot), $N = 100$ (dashed) and $N = 200$ (solid).

The penalization is active and interacts with the numerical solution in the simulation – if length errors start to grow, the penalization term gets larger and will act more strongly to reduce them. This can be viewed as introducing some pulling at discrete points to rearrange them at a uniform spacing in arclength. How the points will be redistributed depends on the solution itself.

A slight shift in the y -position of the filament, as we have gone through the buckling phase, will over time lead to a larger shift in the x -coordinate of the center position, due to the nature of the shear flow. In the end of the simulations, we do not always get a convergence rate close to 2 if we measure the difference between consecutive solutions. In the three set of runs presented in this section, the convergence rate is higher than second order in the end of the simulations. For other simulations, convergence rates might be smaller than 2 instead. However, if we center the three solutions for the filament coordinates at the origin, we do measure close to second-order convergence. At the late time $t = 61.44$, we have an order of convergence of 1.97.

4.2. Interacting filaments

In rheological experiments for fiber suspensions, a stationary or oscillatory shearing background flow is often imposed. One can measure properties such as the stress response and the time scale for this response and the distribution of fiber orientations.

Below, we present a simulation where 25 filaments of equal length are inserted into an oscillatory background shear flow. Periodic boundary conditions are imposed in the streamwise (x) direction. In Fig. 1, we defined the angle θ in the xy -plane such as, for the steady flow, the straight filament in the plane is under compression for $\pi > \theta > \pi/2$, and under extension for $\pi/2 > \theta > 0$. In the oscillatory flow, this is true for the first half of each period, where as the situation will be reversed in the second half period, when the flow is in the opposite direction. Hence, filaments that are under compression will become under extension when the flow reverses, and vice versa.

The parameters are $\bar{\mu} = 1.5 \times 10^5$ and $\varepsilon = 10^{-2}$. We use $N = 100$ points to discretize each filament, and a time step $\Delta t = 0.0128$. We define the background shear flow $\mathbf{U}_0 = (\sin(2\pi\omega t)y, 0, 0)$, where $\omega = (2000\Delta t)^{-1}$, so that one period is 2000 time steps.

To impose the periodicity in the x -direction, we make use of the approximation introduced in Eq. (42). The accuracy of this approximation is investigated in Appendix C. We define the periodic interval in x to be of length 2 (twice the filament length).

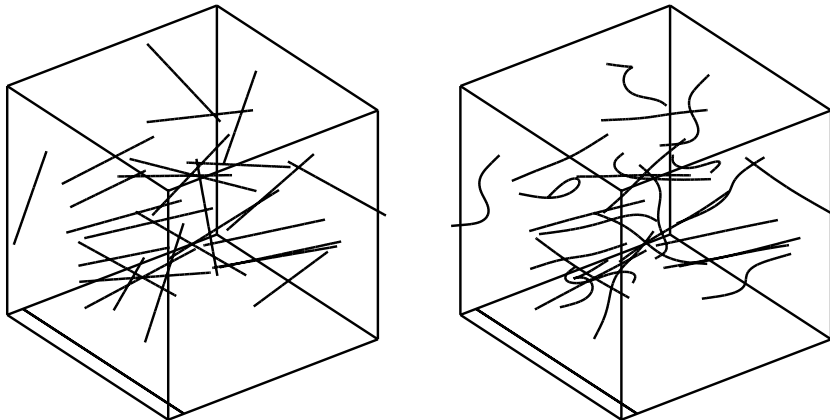


Fig. 10. Filament configurations at $t = 0.0$ and $t = 25.6$. The velocity $\mathbf{U}_0 = (\sin(2\pi\omega t)y, 0, 0)$ is zero at these points in time.

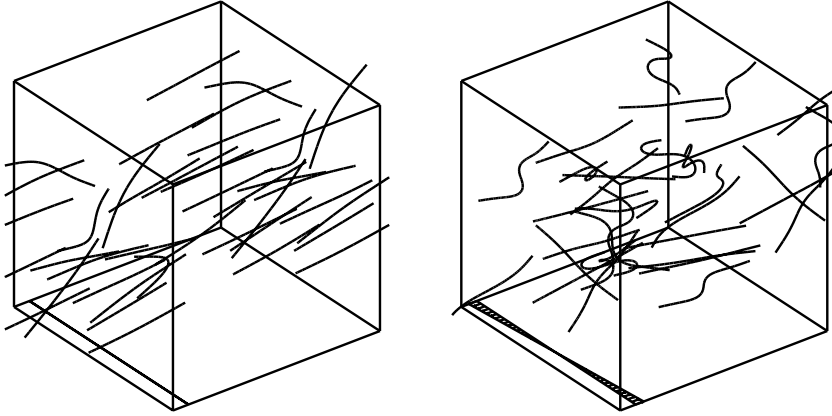


Fig. 11. Filament configurations at $t = 38.4$ and 49.024 . The velocity profile of the background shear flow $U_0 = (\sin(2\pi\omega t)y, 0, 0)$ is indicated at the bottom.

The initial filament configuration is shown in the left plot in Fig. 10. All filaments are of length 1, and are initially straight. In the case of one single filament in Section 4.1, we introduced a small perturbation to the straight filament to excite buckling. In this case, the filament interactions will be sufficient for this purpose. In the right plot in Fig. 10, the filament configuration is shown after one period, at $t = 25.6$. In Fig. 11, the filament configurations at $t = 38.4$ and 49.024 are plotted.

When the filaments buckle, they store elastic energy that can later be released back to the system. The total elastic energy is defined as

$$E_{\text{elas}} = \sum_{k=1}^{25} \frac{1}{2} \int_{\Gamma_k} |(\mathbf{x}_k)_{,ss}|^2 ds, \quad (49)$$

where $|(\mathbf{x}_k)_{,ss}|$ is the curvature of filament k as a function of arclength s . In particular, E_{elas} is proportional to the trace of the bending part of the extra stress tensor (Eq. (48)). E_{elas} is plotted in Fig. 12 versus time for five periods of the oscillating shear.

In the plot of the elastic energy (Fig. 12), we can see that the elastic energy has a peak around $t = 23.3$. At this time, many filaments are strongly bent, after which they start to relax as the flow slows down. At $t = 25.6$ (configuration plotted in Fig. 10), the background velocity is zero, and the flow is changing direction. At $t = 38.4$ (Fig. 11) after one and a half period, there is little elastic energy in the system. Many filaments are close to being straight, and the ones that are bent show only moderate bending. On the other

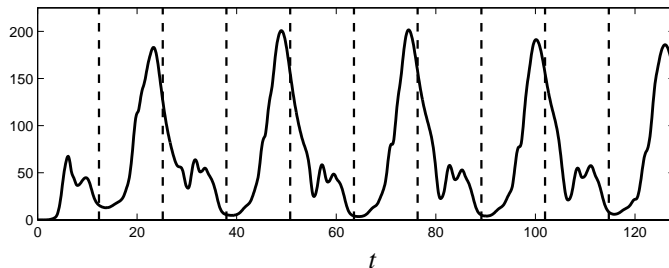


Fig. 12. Total elastic energy E_{elas} as defined in Eq. (49) plotted versus time t . The period for the oscillating shear flow is 25.6, and the dashed lines marks each half-period, i.e. the points in time when the background flow changes direction.

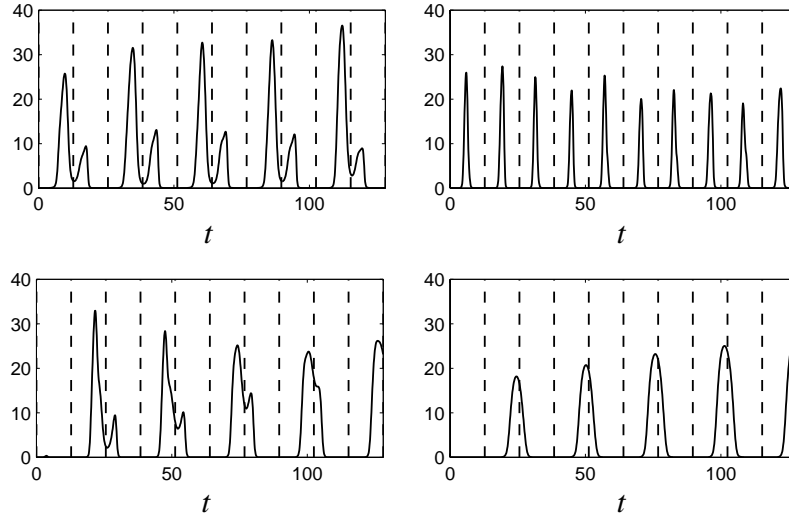


Fig. 13. Elastic energy plotted versus time t for four different filaments. The total elastic energy is plotted in Fig. 12.

hand, by $t = 49.024$ (Fig. 11), many filaments are again buckled strongly, and at this point, the system has its maximum elastic energy within the second period.

In Fig. 13, we plot the elastic energy for four different filaments as a function of time. These four filaments all develop rather high curvatures at some points in time. Viewing this as a sample of possible evolutions, we see that there are filaments that buckle strongly in the first half period, and very little in the second, or vice versa. There are also filaments that buckle to about the same degree in both the first and the second half period. For some filaments, the maximum energy over one full period decays in later periods, while it increases for others. Large elastic energies are for example found for filaments with an initial position and orientation such that they undergo a small buckling in the first half-period of the oscillations. As the direction of the flow changes, they have not been under extension long enough to get completely straight, and still hold slightly bent shapes. They therefore bend strongly as they get under compression when the flow direction changes, leading to a peak in the elastic energy in the second half-period. Two examples of the elastic energies of such filaments are found in the two lower plots in Fig. 13.

In a system of 25 filaments, the total elastic energy depends strongly on the initial configuration, suggesting that the number of filaments is as yet too small to get a good distribution of positions and orientations.

Other interesting phenomena to study for suspensions are filament orientation, suspension viscosity as a function of volume fraction and flexibility of the fibers, and normal stress differences. In the simulation presented here, all filaments are of equal length, and it is also interesting to study the effect of different length distributions of the filaments on the above mentioned properties.

Considering first normal stress differences, we find that already one single filament that buckles in the plane yields a positive integrated first normal stress, which is not the case if buckling does not occur. As discussed in Section 4.1, there is no configuration that can yield a negative normal stress contribution that cancels that positive contribution. Hence, even in dilute suspensions of fibers, where the interactions between filaments are weak, the buckling of the fibers will yield a net positive first normal stress difference.

It is also possible to extract information and there from compute bulk properties of the suspension. However, in order for these bulk properties to be representative for a filament suspension, the simulations must include a larger number of filaments.

To include the interactions of the filaments, we need to compute the contribution from $M - 1$ other filaments for each filament, or from $3M - 2$ filaments if we as in this case include a periodic layer of boxes in the streamwise direction (the cost to compute the approximate terms in the periodic sum is negligible). This yields that the cost to compute the interactions grows proportional to M^2 .

The time-step size is proportional to $1/N$, where N is the number of points on the filament, and so the number of time steps is proportional to N . In each time step, the leading order terms of the computational cost are $C_1MN^3 + C_2M^2N^2$. The first term comes from solving separate systems for the M filaments for both the implicitly discretized dynamics equation and the line tension equation, with the number of unknowns proportional to N . The second term comes from computing the interaction between the different filaments. When the number of filaments is small, the first term dominates, but as the number of filaments grow, the computation for the interactions take up a majority of the computational time.

The next step in the development of the numerical algorithm is therefore to make this summation procedure more efficient, using modern fast summation strategies [9,29,37]; thereby reducing the cost of this part to $O(MN \log(MN))$ or even $O(MN)$.

5. Concluding remarks

We have developed a formulation, based on slender body asymptotics, for simulating the non-local hydrodynamics of slender flexible fibers immersed in an incompressible Stokesian fluid. The mathematical description has the form of a system of integral equations along the filament centerlines and takes into account the influence of all fluid–filament and filament–filament interactions. This formulation is also appropriately regularized, with no loss of asymptotic accuracy, so as to satisfy a solvability condition and to control possible instabilities occurring at length-scales below those described by a slender body approximation.

The numerical method is based on finite differences to compute derivatives in space and time, implicit time-stepping, and product integration to treat the integral terms. The numerical quadrature procedure is carefully designed to resolve rapidly changing terms and to achieve a good cancellation between the different parts of the integral operators. We have demonstrated the ability of our method to simulate flows with many interacting filaments and where substantial buckling of the filaments occur. We have shown the second-order convergence of the method, and that length errors are well controlled when the line tension equation is stabilized with the penalization term.

This method can be applied to several very interesting fluid dynamics problems. Our simulations here have given new results on the fundamental behaviors of single and multiple interacting filaments in steady and oscillating shear flow, showing in particular the development of complicated shape perturbations and the storage and release of elastic stress. Becker and Shelley [4] used a local drag model to identify a sharp transition to buckling for a single elastic filament in shear, arguing that this transition was associated with the development of first normal stress differences. While the point of transition showed good agreement with experiments, the growth of stresses did not. This discrepancy may be due to the lack of filament–filament interactions in their model, a point we can now begin to address by investigating the growth of stresses past a buckling transition as a function of filament concentration. An important element in doing this will be increasing the number of filaments in our simulations.

Another very interesting, and very current, set of problems starts with the discoveries that fluids can be mixed efficiently at low Reynolds number by using viscoelastic fluids [17,18], and that such fluids can be used for control of microfluidic devices [16]. Important elements underlying such technological possibilities are the nonlinearities and additional time-scales associated with elastic response. Models based upon the nonlinear interactions of elastic filaments with background flows, and with each other, could shed light on the basic mechanisms.

In order to increase the number of filaments in our simulations, there are two main improvements to be made. The first is to implement a fast summation strategy, such as is done for potential flows [15], for evaluating the Stokeslets and doublets arising from discretization of the filament–filament interactions. Of particular interest here are the recent advances in the area of “kernel-independent” methods which are readily adapted to a variety of summation kernels [9,29,37]. The second is to parallelize the method. This is rather straightforward as most of the computations are done on each filament separately, and interaction terms are treated in an explicit manner.

In this paper, we have considered only rather dilute suspensions, and have not focused much on the very near interactions of two filaments. In near-range interactions, lubrication forces are active and need to be modeled more accurately. One possible approach is to represent filament surfaces explicitly in the region of nearby filament interactions, perhaps within the context of a boundary integral representation of surface velocity, and treat the “far-field” via slender body asymptotics.

Acknowledgements

This work was supported in part by DOE Grant No. DE-FG02-88ER25053 and NSF Grant No. DMS-9980069.

Appendix A. Finite difference formulas

The filament centerlines are discretized uniformly in the arclength s , with N intervals, i.e. with grid size $h = 1/N$. The discrete points are given by $s_j = jh$, $j = 0, \dots, N$, and we use the notation $f_j = f(s_j)$.

We introduce divided difference operators D_p , so that $D_p f_j$ approximates the derivatives $f^{(p)}(s_j)$ to an $O(h^2)$ error, for $p = 1, \dots, 4$. The standard centered operators are used whenever possible, but at boundaries we apply skew operators. We define:

$$D_1 f_j = \begin{cases} (-f_{j+2} + 4f_{j+1} - 3f_j)/(2h), & j = 0, \\ (f_{j+1} - f_{j-1})/(2h), & 1 \leq j \leq N-1, \\ (3f_j - 4f_{j-1} + 2f_{j-2})/(2h), & j = N. \end{cases} \quad (\text{A.1})$$

$$D_2 f_j = \begin{cases} (-f_{j+3} + 4f_{j+2} - 5f_{j+1} + 2f_j)/h^2, & j = 0, \\ (f_{j+1} - 2f_j + f_{j-1})/h^2, & 1 \leq j \leq N-1, \\ (2f_j - 5f_{j-1} + 4f_{j-2} - f_{j-3})/h^2, & j = N. \end{cases} \quad (\text{A.2})$$

$$D_3 f_j = \begin{cases} (-\frac{3}{2}f_{j+4} + 7f_{j+3} - 12f_{j+2} + 9f_{j+1} - \frac{5}{2}f_j)/h^3, & j = 0, \\ (-\frac{1}{2}f_{j+3} + 3f_{j+2} - 6f_{j+1} + 5f_j - \frac{3}{2}f_{j-1})/h^3, & j = 1, \\ (f_{j+2} - 2f_{j+1} + 2f_{j-1} - f_{j-2})/(2h^3), & 2 \leq j \leq N-2, \\ (\frac{3}{2}f_{j+1} - 5f_j + 6f_{j-1} - 3f_{j-2} + \frac{1}{2}f_{j-3})/h^3, & j = N-1, \\ (\frac{5}{2}f_j - 9f_{j-1} + 12f_{j-2} - 7f_{j-3} + \frac{3}{2}f_{j-4})/h^3, & j = N. \end{cases} \quad (\text{A.3})$$

$$D_4 f_j = \begin{cases} (-2f_{j+5} + 11f_{j+4} - 24f_{j+3} + 26f_{j+2} - 14f_{j+1} + 3f_j)/h^4, & j = 0, \\ (-f_{j+4} + 6f_{j+3} - 14f_{j+2} + 16f_{j+1} - 9f_j + 2f_{j-1})/h^4, & j = 1, \\ (f_{j+2} - 4f_{j+1} + 6f_j - 4f_{j-1} + f_{j-2})/h^4, & 2 \leq j \leq N-2, \\ (2f_{j+1} - 9f_j + 16f_{j-1} - 14f_{j-2} + 6f_{j-3} - f_{j-4})/h^4, & j = N-1, \\ (3f_j - 14f_{j-1} + 26f_{j-2} - 24f_{j-3} + 11f_{j-4} - 2f_{j-5})/h^4, & j = N. \end{cases} \quad (\text{A.4})$$

Appendix B. Regularization

B.1. Analysis for the straight filament case

We here analyze the unregularized equation for the case where the filament is straight, and Eq. (13) for $T(s)$ simplifies greatly. The unit tangent vector \mathbf{x}_s is then constant, and all higher derivatives of \mathbf{x} are zero. The equation reads

$$2cT_{ss} - \mathbf{x}_s \cdot \frac{\partial}{\partial s} \mathbf{K}[T_s \mathbf{x}_s] = \bar{\mu} \mathbf{x}_s \cdot \frac{\partial}{\partial s} \mathbf{U}_0. \quad (\text{B.1})$$

Using that in this case, $\hat{\mathbf{R}}\hat{\mathbf{R}} = \hat{\mathbf{s}}\hat{\mathbf{s}}$ and $|\mathbf{R}| = |s - s'|$ in the definition (4) of $\mathbf{K}[\mathbf{f}]$, Eq. (B.1) becomes

$$\bar{\mu} \mathbf{x}_s \cdot \frac{\partial}{\partial s} \mathbf{U}_0 = 2 \frac{\partial}{\partial s} \left(cT_s - \int_0^1 \frac{T_s(s') - T_s(s)}{|s' - s|} ds' \right).$$

This equation can be integrated to read

$$cT_s - \int_0^1 \frac{T_s(s') - T_s(s)}{|s' - s|} ds' = g(s), \quad (\text{B.2})$$

where $g(s)$ is some scalar function of s .

Götz [14] has showed that the operator

$$S[\varphi](\alpha) = \int_{-1}^1 \frac{\varphi(\alpha') - \varphi(\alpha)}{|\alpha' - \alpha|} d\alpha' \quad (\text{B.3})$$

is diagonalizable by the Legendre polynomials P_n , i.e.

$$S[P_n] = -\lambda_n P_n \quad \forall n \in N_0, \quad (\text{B.4})$$

where the eigenvalues λ_n are given by

$$\lambda_n = 2 \sum_{i=1}^n 1/i, \quad n > 0 \text{ and } \lambda_0 = 0. \quad (\text{B.5})$$

Asymptotically, $\lambda_n \rightarrow 2(\log n + \gamma)$ where $\gamma = 0.57721 \dots$ (Euler's constant) as $n \rightarrow \infty$.

With $s = (\alpha + 1)/2$, defining $\vartheta(\alpha) = T_s(s)$, Eq. (B.2) can be written as

$$c\vartheta(\alpha) - S[\vartheta](\alpha) = g\left(\frac{\alpha + 1}{2}\right).$$

Expanding ϑ and g on the Legendre polynomials P_n , and using relation (B.4) we find that this continuous problem will not have a solution unless

$$c + \lambda_n \neq 0 \quad \forall n. \quad (\text{B.6})$$

For $n = 0$, $\lambda_n = 0$, and since $c = \log(\varepsilon^2 e) < 0$, $c + \lambda_0 < 0$. As n gets large, $c + \lambda_n \rightarrow \log(\varepsilon^2 e) + 2 \log n + 2\gamma = 2 \log(\sqrt{e} \varepsilon n) + 2\gamma = 2 \log(\sqrt{e} e^\gamma \varepsilon n)$. Hence, for large enough n , $c + \lambda_n$ will be positive for a fixed small ε . For some n , we might therefore have $c + \lambda_n$ equal to, or very close to 0.

In Fig. 14 λ_n has been plotted as a function of n . Overlaid in the figure are lines for $-c$ for $\varepsilon = 10^{-2}$, 10^{-3} and 10^{-4} . The λ_n curve passes the $-c$ level as $c + \lambda_n$ goes from negative to positive. For $\varepsilon = 10^{-2}$, the value of $c + \lambda_n$ is negative for $n = 33$ and positive for $n = 34$. For $\varepsilon = 10^{-4}$, we have $n = 3404$ and 3405 , respectively.

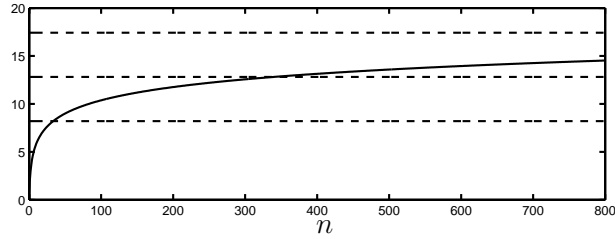


Fig. 14. λ_n as defined by (B.5) plotted versus n . The dashed lines indicate the values of $-c = -\log(\varepsilon^2 e)$ for $\varepsilon = 10^{-2}$, 10^{-3} and 10^{-4} from the bottom and up.

Expanding a function in terms of Legendre polynomials, finer scales are resolved as more polynomials are included, i.e. as n increases. One can view the solvability condition (B.6) as a constraint not to resolve scales smaller than the ε -scale, which are the length-scales below those captured by the slender body theory. The n value for which the quantity $\lambda_n + c$ turns positive is approximately proportional to $1/\varepsilon$. For very small values of ε , the asymptotic value of λ_n yields that this occurs at $n > e^{-\frac{1}{2}\gamma} \varepsilon^{-1}$.

Even if the condition is discrete, and could be avoided by a clever choice of ε , the condition will change as a filament becomes non-straight, and thus there is no such choice that safely avoids the solvability condition being violated. In practice, the solvability condition sets a limit on what resolution can be used to discretize the problem. For larger ε , like $\varepsilon = 10^{-2}$, where the permitted resolution is the lowest ($n < 34$ was found above), this would not be sufficient to resolve the shape of the filament during the course of a simulation, even as it attains a moderate curvature. The line tension equation is derived from the equation for the velocity of the filament centerline, and so there are naturally related problems with the evolution equation. For the case of a closed loop in the plane, Shelley and Ueda [33] studied the time dependent slender body equations and noted that the jump discontinuity in the kernel gives rise to a high wave number instability at sufficiently high wave numbers, beyond $k \sim 1/\varepsilon$. In short, the original equations are not suitable for numerical discretization.

B.2. Regularization of the integral operator

As a remedy for making their equations suitable for numerical simulations, Shelley and Ueda [33] suggested a regularization of the integral operator as in Eq. (15), but with a constant δ . They furthermore showed, that for a closed filament, the regularized integral operator \mathbf{K}_δ in Eq. (15) with δ constant differs from the unregularized one ($\delta = 0$) by $O(\delta^2 \log \delta)$. Therefore, if $\delta \sim \varepsilon$, the asymptotic accuracy of the slender body equations with the original operator replaced by the regularized one is still $O(\varepsilon^2 \log \varepsilon)$, i.e. the two formulations are asymptotically equivalent.

However, in our case, the curve is not closed, and we have to consider the general case of a filament with free ends. The analysis in this case shows that while the regularization again modifies $\mathbf{K}[\mathbf{f}](s)$ to $O(\delta^2 \log \delta)$ if s is in the interior, the modification is only $O(\delta)$ as s approaches one of the free ends. This alters the asymptotic accuracy (if $\delta \sim \varepsilon$) of the regularized equations, which we would like to avoid.

Instead, we replace the constant δ by a variable $\delta(s)$. With $\delta(s) = \delta_0 \phi(s)$, where $\phi(s)$ is such that $\phi(s)/s$ and $\phi(s)/(1-s)$ are uniformly bounded, the regularization introduces a modification of $O(\delta_0^2 \log \delta_0)$. With $\delta_0 \sim \varepsilon$, this again yields a formulation that is asymptotically equivalent to the original formulation. An outline of this proof is given in the next section of this appendix. One possible choice of $\phi(s) \in C^1(s)$ is given in Eq. (16).

So, is a choice of $\delta \sim \varepsilon$ sufficient to remove the solvability condition? To answer this question, we return again to the line tension equation (Eq. (13)). Here, we can note the presence of the second-order term $2cT_{ss}$, but also that there is another such term hidden in the integral operator. With $\delta = 0$, the integral in Eq. (15)

is only defined when both terms are included, and none of the terms in the integral can be evaluated by them selves. With $\delta > 0$ however the second term in the integral can be written as

$$-(\mathbf{I} + \hat{\mathbf{s}}(s)\hat{\mathbf{s}}(s))\mathbf{f}(s) \int_0^1 \frac{1}{\sqrt{|s-s'|^2 + \delta^2}} ds' = -(\mathbf{I} + \hat{\mathbf{s}}(s)\hat{\mathbf{s}}(s))\mathbf{f}(s)\varphi(s),$$

where $\varphi(s) = \log((s + \sqrt{s^2 + \delta^2})(1 - s + \sqrt{(1-s)^2 + \delta^2})/\delta^2)$. Using this, it can be noted that in the line tension equation, the term $-\mathbf{x}_s \cdot (\partial/\partial s)\mathbf{K}_\delta^0[(T\mathbf{x}_s)_s]$, yields among others a term $2\varphi(s)T_{ss}$. Adding this to the original elliptic term, the coefficient is $2(c + \varphi(s))$. This expression will be smaller than zero for all values of s only if $\delta > \sqrt{\epsilon\epsilon}$. If δ is smaller than this limit, there will be some value for s for which the coefficient is zero, and the ellipticity of the equation is destroyed. This is by no means a complete analysis, but numerical tests confirm the result, that this is the limit for sufficient regularization.

Also in the case with a variable $\delta(s)$, numerical experiments show that with $\delta_0 > \sqrt{\epsilon\epsilon}$, this variable $\delta(s)$ provides enough regularization to remove the solvability condition.

B.3. Asymptotic equivalence

Let $\mathbf{K}_\delta[\mathbf{f}](s)$ be defined as in Eq. (15) with $\delta(s) = \delta_0\phi(s)$. Assume $|\phi(s)| \leq 1$, and $\phi(s) \in C(\mathbb{R})$ with $\phi(s)/s$ and $\phi(s)/(1-s)$ uniformly bounded. Let $\mathbf{K}_0[\mathbf{f}](s)$ be defined as in Eq. (15) with $\delta = 0$. Then, we have that

$$|\mathbf{K}_\delta[\mathbf{f}](s) - \mathbf{K}_0[\mathbf{f}](s)| \leq C\delta_0^2 \log \delta_0. \tag{B.7}$$

The outline for how this can be shown follows below.

Let us subtract and add a term to the integral operator, and then split it into two parts, $\mathbf{K}_\delta[\mathbf{f}](s) = I_1(s) + I_2(s)$, where

$$I_1(s) = \int_0^1 \left[\frac{\mathbf{I} + \hat{\mathbf{R}}\hat{\mathbf{R}}}{\sqrt{|\mathbf{R}|^2 + \delta(s)^2}} - \frac{\mathbf{I} + \hat{\mathbf{s}}\hat{\mathbf{s}}}{\sqrt{(s-s')^2 + \delta(s)^2}} \right] \mathbf{f}(s') ds', \tag{B.8}$$

$$I_2(s) = (\mathbf{I} + \hat{\mathbf{s}}\hat{\mathbf{s}}) \int_0^1 \frac{\mathbf{f}(s') - \mathbf{f}(s)}{\sqrt{(s-s')^2 + \delta(s)^2}} ds'. \tag{B.9}$$

For each of $I_1(s)$ and $I_2(s)$, we will split the integral into sub-intervals, taking out the interval where s' is close to s to be treated separately. The integrals are split into the following sub-intervals:

$$\int_0^1 = \begin{cases} \int_0^{s+\omega} + \int_{s+\omega}^1, & s < \omega, \\ \int_0^{s-\omega} + \int_{s-\omega}^{s+\omega} + \int_{s+\omega}^1, & \omega \leq s \leq 1 - \omega, \\ \int_0^{s-\omega} + \int_{s-\omega}^1, & s > 1 - \omega, \end{cases} \tag{B.10}$$

where $\omega = (1/2) \min(\omega_1, \omega_2, \omega_3, \dots) \geq C > 0$. Here, ω_i is the radius of convergence for expansion of components of \mathbf{f} and \mathbf{x} , assumed sufficiently differentiable.

We start by considering $I_2(s)$. In the case when $|s-s'| \geq \omega$, the difference between the regularized and unregularized integral can be found by Taylor expansion. In the case where $|s-s'| < \omega$, we again Taylor expand, and then make use of the recursive formula

$$\int \frac{\alpha^p}{\sqrt{\alpha^2 + \delta(s)^2}} d\alpha = \frac{1}{p} \left[\alpha^{p-1} \sqrt{\alpha^2 + \delta(s)^2} - (p-1)\delta(s)^2 \int \frac{\alpha^{p-2}}{\sqrt{\alpha^2 + \delta(s)^2}} d\alpha \right].$$

From here, we need to show the closeness of the first part to the unregularized result, and the boundedness of the second part. Again, we Taylor expand. A special case is where $s < \omega$ or $s > 1 - \omega$. In this case, we need the use the assumption that $\phi(s)/s$ and $\phi(s)/(1-s)$ are uniformly bounded, to get the result of $O(\delta_0^2)$. Now, turn to $I_1(s)$. We rewrite this integral as was done in Eqs. (31) and (32).

We need to compare the result of this integral to the unregularized result with $\delta = 0$. Again, we follow the same route, although the Taylor expansions are more involved. In this case, after Taylor expanding in the case where $|s - s'| < \omega$, we apply the more general recursive formula

$$\int \frac{\alpha^{j+2i}}{(\alpha^2 + \delta(s)^2)^{i+1/2}} d\alpha = \frac{1}{j} \frac{\alpha^{j+2i-1}}{(\alpha^2 + \delta^2)^{i-1/2}} - \delta(s)^2 \frac{j+2i-1}{j} \int \frac{\alpha^{j+2i-2}}{(\alpha^2 + \delta(s)^2)^{i+1/2}} d\alpha.$$

Again, we need to show the closeness of the first part of the unregularized result, and the boundedness of the recursive terms.

For most parts, the regularized integral differs from the unregularized by $O(\delta_0^2)$. However, one recursive term in the expansion of $I_2(s)$ as well as of $I_1(s)$ is only bounded by a constant times $\delta_0^2 \log \delta_0$. Hence, in total, we find that $|\mathbf{K}_\delta[\mathbf{f}](s) - \mathbf{K}_0[\mathbf{f}](s)| \leq C\delta_0^2 \log \delta_0$.

Appendix C. Numerical test of periodicity

In Section 3.4, we discussed the evaluation of the periodic sum (40). In Eq. (42), we introduced an approximation to this sum in which we included the terms for $p = -1, 0, 1$, and approximations for $2 \leq |p| \leq Q$. In this section, we want to study the quality of this approximation.

Given a filament shape and the corresponding line tension at some time, we compute the following vector valued sums at a set of test points:

$$\Sigma_{\text{ref}}(\bar{\mathbf{x}}) = \sum_{p=-P}^P \mathbf{V}^p(\bar{\mathbf{x}}), \quad \tilde{\Sigma}_C(\bar{\mathbf{x}}) = \sum_{p=-1}^1 \mathbf{V}^p(\bar{\mathbf{x}}), \quad \tilde{\Sigma}_Q(\bar{\mathbf{x}}) = \tilde{\Sigma}_C(\bar{\mathbf{x}}) + \sum_{2 \leq |p| \leq Q} \tilde{\mathbf{V}}^p(\bar{\mathbf{x}}).$$

The filament, which in this test lies in the xy -plane, and its two closest periodic images are plotted in Fig. 15. The periodicity is in the x -direction, with the period length $d_1 = 2$. The filament is discretized with $N = 200$ points, and the integrals are evaluated using the trapezoidal rule. The test points are placed along a vertical line, $-0.8 \leq y \leq 0.8$, with x -coordinate \bar{x} .

In Fig. 16, $|\Sigma_{\text{ref}}(\bar{x}, y, 0)|$ is plotted versus y for three different values of \bar{x} . The term has been scaled by $1/\bar{\mu}$. The magnitude decreases as we place the test points further away from the filament, up until the next periodic image becomes the closest one.

If we include only the contributions for $p = -1, 0, 1$ in the sum, as in $\tilde{\Sigma}_C(\bar{\mathbf{x}})$, the relative error can be rather large, as can be seen in Fig. 17. As long as the test points are much closer to one copy of the filament

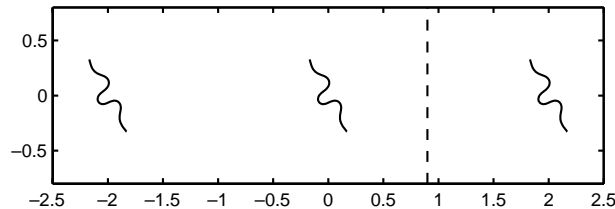


Fig. 15. A filament and its closest two periodic images. The vertical dashed line indicates the line with $x = \bar{x}$ along which we place the test points.

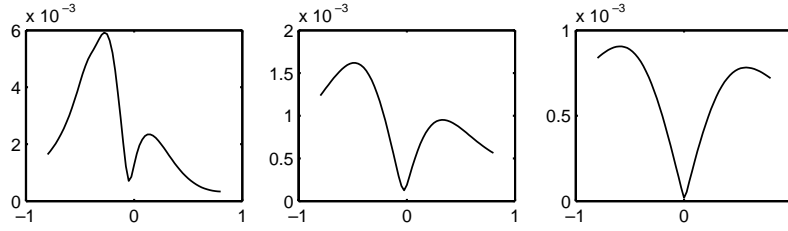


Fig. 16. $|\Sigma_{\text{ref}}(\bar{x}, y, 0)|$ plotted versus y for, from left to right $\bar{x} = 0.3, 0.6$ and 0.9 .

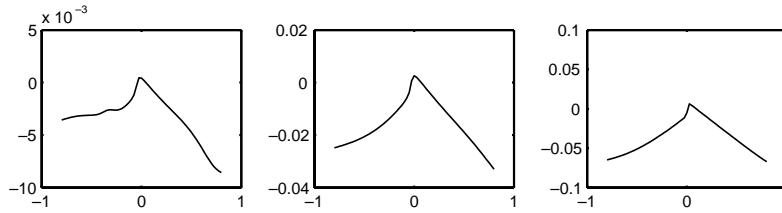


Fig. 17. $(|\tilde{\Sigma}_C(\bar{x}, y, 0) - \Sigma_{\text{ref}}(\bar{x}, y, 0)|) / \max_y |\Sigma_{\text{ref}}(\bar{x}, y, 0)|$ plotted versus y for, from left to right $\bar{x} = 0.3, 0.6$ and 0.9 .

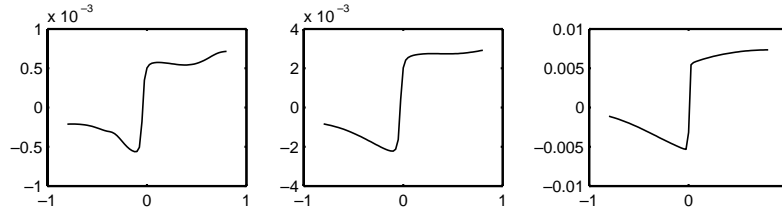


Fig. 18. $(|\tilde{\Sigma}_Q(\bar{x}, y, 0) - \Sigma_{\text{ref}}(\bar{x}, y, 0)|) / \max_y |\Sigma_{\text{ref}}(\bar{x}, y, 0)|$ plotted versus y for, from left to right $\bar{x} = 0.3, 0.6$ and 0.9 .

than to the others, this contribution dominates, and the sum is also well balanced, and the error is rather small. For $\bar{x} = 0.9$ however the test points are about the same distance from two copies of the filament, and the largest relative error is 6.7%. If we add the contribution for $p = 2$ to the sum, the error decreases to 3.4%.

In this discussion, we should however remember that when the closest distance between say filaments 1 and 2 is large, the contribution from filament 2 to filament 1 will be small compared to other contributions, such as from filament 1 itself. Therefore, an error of 6.7%, although not satisfactory, is not catastrophic.

When we add the sum of approximative terms to the truncated sum, as in $\tilde{\Sigma}_Q(\bar{x})$, the error is significantly decreased, as can be seen by comparing the plots in Fig. 18 to the ones in Fig. 17. Also here, the largest error is naturally found for $\bar{x} = 0.9$, but in this case it is much smaller, about 0.7%.

Several different tests have been made with different shaped filaments, different layouts, etc. The filament in our test here has a rather high curvature. For filaments that are less bent, the periodic approximation works even better. It also improves more if the length of the periodic interval is increased.

To conclude, we have seen that an addition of our periodic approximation significantly improves the result compared to simply truncating the sum. This is done to a very low cost, since once the integral in Eq. (41) has been evaluated, the result can be used to compute the approximation $\tilde{\mathbf{V}}^p(\bar{x})$ for any \bar{x} and p . If evaluating the exact contribution, $\mathbf{V}^p(\bar{x})$, the integral must be recomputed for each new \bar{x} and p .

References

- [1] K.E. Atkinson, *An Introduction to Numerical Analysis*, Wiley, New York, 1989.
- [2] G.K. Batchelor, *An Introduction to Fluid Dynamics*, Cambridge University Press, Cambridge, 1967.
- [3] G.K. Batchelor, The stress system in a suspension of force-free particles, *J. Fluid Mech.* 41 (1970) 545–570.
- [4] L. Becker, M. Shelley, The instability of elastic filaments in shear flow yields first normal stress differences, *Phys. Rev. Lett.* 87 (2001) 198301.
- [5] M.E. Cates, S.J. Candau, Statics and dynamics of worm-like surfactant micelles, *J. Phys.: Condens. Matter* 2 (1990) 6869–6892.
- [6] S. Childress, *Mechanics of Swimming and Flying*, Cambridge University Press, Cambridge, 1981.
- [7] A.T. Chwang, T.Y.-T. Wu, Hydrodynamics of low-Reynolds-number flow. Part 2. Singularity method for stokes flow, *J. Fluid Mech.* 67 (1975) 787.
- [8] X. Fan, N. Phan-Thien, R. Zheng, A direct simulation of fibre suspensions, *J. Non-Newtonian Fluid Mech.* 74 (1998) 113–135.
- [9] Z. Gimbutas, V. Rokhlin, A generalized fast multipole method for nonoscillatory kernels, *SIAM J. Sci. Comp.* 24 (2002) 796–817.
- [10] T. Gisler, D.A. Weitz, Scaling of the microrheology of semidilute F-Actin solutions, *Phys. Rev. Lett.* 82 (1999) 1606–1609.
- [11] R. Goldstein, S. Langer, Nonlinear dynamics of stiff polymers, *Phys. Rev. Lett.* 75 (1995) 1094.
- [12] R. Goldstein, T. Powers, C. Wiggins, Viscous nonlinear dynamics of twist and writhe, *Phys. Rev. Lett.* 80 (1998) 5232.
- [13] S. Goto, H. Nagazono, H. Kato, Polymer solutions. 1: Mechanical properties, *Rheol. Acta* 25 (1986) 119–129.
- [14] T. Götz, Interactions of fibers and flow: asymptotics, theory and numerics, Ph.D. Thesis, University of Kaiserslautern, Germany, 2000.
- [15] L. Greengard, V. Rokhlin, A fast algorithm for particle simulations, *J. Comput. Phys.* 73 (1987) 325–348.
- [16] A. Groisman, M. Enzelberger, S. Quake, Microfluidic memory and control devices, *Science* 300 (2003) 955–958.
- [17] A. Groisman, V. Steinberg, Elastic turbulence in a polymer solution flow, *Nature* 405 (2000) 53.
- [18] A. Groisman, V. Steinberg, Efficient mixing at low Reynolds numbers using polymer additives, *Nature* 410 (2001) 905.
- [19] A. Jayaraman, A. Belmonte, Oscillations of a solid sphere falling through a wormlike micellar fluid, *Phys. Rev. E* 67(6) (2003), Art. No: 065301.
- [20] G.B. Jeffery, The motion of ellipsoidal particles immersed in viscous fluid, *Proc. R. Soc. Lond. A* 102 (1922) 161–179.
- [21] R.E. Johnson, An improved slender-body theory for stokes flow, *J. Fluid Mech.* 99 (1980) 411–431.
- [22] C.G. Joung, N. Phan-Thien, X. Fan, Direct simulation of flexible fibers, *J. Non-Newtonian Fluid Mech.* 99 (2001) 1–36.
- [23] J. Keller, S. Rubinow, Slender-body theory for slow viscous flow, *J. Fluid Mech.* 75 (1976) 705–714.
- [24] R.G. Larson, *The Structure and Rheology of Complex Fluids*, Oxford University Press, Oxford, 1998.
- [25] S. Lim, C.S. Peskin, Simulations of the wirling instability by the immersed boundary method, *SIAM J. Sci. Comput.* (to appear).
- [26] A. Mayo, C. Peskin, An implicit numerical method for fluid dynamics problems with immersed elastic boundaries, *Contemp. Math.* 141 (1993) 261–277.
- [27] P. Palfy-Muhoray, B. Bergersen, H. Lin, R. Meyer, Z. Racz, Filaments in liquid crystals: structure and dynamics, in: S. Kai (Ed.), *Pattern Formation in Complex Dissipative Systems*, World Scientific, Singapore, 1991.
- [28] C.S. Peskin, The immersed boundary method, *Acta Numer.* 11 (2002) 479–517.
- [29] J. Phillips, J. White, A precorrected-fft method for electrostatic analysis of complicated 3d structures, *IEEE Trans. Computer-Aided Des. Integrated Circuits Syst.* 16 (1997) 1059–1072.
- [30] C. Pozrikidis, *Boundary Integral and Singularity Methods for Linearized Viscous Flow*, Cambridge University Press, Cambridge, 1992.
- [31] L. Segel, *Mathematics Applied to Continuum Mechanics*, MacMillan, New York, 1977.
- [32] M. Shelley, T. Ueda, The nonlocal dynamics of stretching, buckling filaments, in: D. Papageorgiou, Y. Renardi (Eds.), *Multi-Fluid Flows and Instabilities*, AMS-SIAM, 1996.
- [33] M.J. Shelley, T. Ueda, The stokesian hydrodynamics of flexing, stretching filaments, *Physica D* 146 (2000) 221–245.
- [34] P. Skjetne, R.F. Ross, D.J. Klingenberg, Simulation of single fiber dynamics, *J. Chem. Phys.* 107 (1997) 2108–2121.
- [35] J.M. Stockie, Simulating the motion of flexible pulp fibres using the immersed boundary method, *J. Comput. Phys.* 147 (1998) 147–165.
- [36] S. Yamamoto, T. Matsuoka, Dynamic simulations of fiber suspensions in shear flow, *J. Chem. Phys.* 102 (1995) 2254–2260.
- [37] L. Ying, G. Biros, D. Zorin, A kernel independent fast multipole algorithm, Technical Report TR2003-839, Department of Computer Science, Courant Institute, New York University, 2003.